

Manuscript version: Author's Accepted Manuscript

The version presented in WRAP is the author's accepted manuscript and may differ from the published version or Version of Record.

Persistent WRAP URL:

<http://wrap.warwick.ac.uk/163073>

How to cite:

Please refer to published version for the most recent bibliographic citation information. If a published version is known of, the repository item page linked to above, will contain details on accessing it.

Copyright and reuse:

The Warwick Research Archive Portal (WRAP) makes this work by researchers of the University of Warwick available open access under the following conditions.

Copyright © and all moral rights to the version of the paper presented here belong to the individual author(s) and/or other copyright owners. To the extent reasonable and practicable the material made available in WRAP has been checked for eligibility before being made available.

Copies of full items can be used for personal research or study, educational, or not-for-profit purposes without prior permission or charge. Provided that the authors, title and full bibliographic details are credited, a hyperlink and/or URL is given for the original metadata page and the content is not changed in any way.

Publisher's statement:

Please refer to the repository item page, publisher's statement section, for further information.

For more information, please contact the WRAP Team at: wrap@warwick.ac.uk.

1 **Structural basis of Lipopolysaccharide Maturation by the O-Antigen Ligase**

2

3 Khuram U. Ashraf¹, Rie Nygaard¹, Owen N. Vickery^{2,3,#}, Satchal K. Erramilli^{4,#}, Carmen M.
4 Herrera^{5,#}, Thomas H. McConville^{6,#}, Vasileios I. Petrou^{7,8}, Sabrina I. Giacometti¹, Meagan
5 Belcher Dufrisne¹, Kamil Nosol⁴, Allen P. Zinkle¹, Chris L.B. Graham², Michael Loukeris⁹,
6 Brian Kloss⁹, Karolina Skorupinska-Tudek¹⁰, Ewa Swiezewska¹⁰, David I. Roper^{2,1}, Oliver B.
7 Clarke^{1,11}, Anne-Catrin Uhlemann⁶, Anthony A. Kossiakoff⁴, M. Stephen Trent^{5*}, Phillip J.
8 Stansfeld^{2,3*} and Filippo Mancina^{1*}

9

10 ¹Department of Physiology and Cellular Biophysics, Columbia University Irving Medical
11 Center, New York, NY 10032, USA.

12 ²School of Life Sciences, University of Warwick, Coventry, CV4 7AL, UK.

13 ³Department of Chemistry, University of Warwick, Coventry, CV4 7AL, UK.

14 ⁴Department of Biochemistry and Molecular Biology, University of Chicago, Chicago, IL,
15 60637, USA.

16 ⁵Department of Infectious Diseases, College of Veterinary Medicine, University of Georgia,
17 Athens, GA, 30602, USA.

18 ⁶Department of Medicine, Division of Infectious Diseases, Columbia University Medical
19 Center, New York, New York, 10032, USA.

20 ⁷Department of Microbiology, Biochemistry, and Molecular Genetics, New Jersey Medical
21 School, Rutgers Biomedical Health Sciences, Newark, NJ, 07103, USA.

22 ⁸Center for Immunity and Inflammation, New Jersey Medical School, Rutgers Biomedical
23 Health Sciences, Newark, NJ, 07103, USA.

24 ⁹New York Consortium on Membrane Protein Structure, New York Structural Biology
25 Center, 89 Convent Avenue, New York, NY, 10027, USA.

26 ¹⁰Institute of Biochemistry and Biophysics, Polish Academy of Sciences, 02-106 Warsaw,
27 Poland.

28 ¹¹Department of Anesthesiology, Columbia University Irving Medical Center, New York,
29 NY, 10032, USA.

30

31 #These authors contributed equally.

32

33 *Correspondence to be addressed to: strent@uga.edu (M.S.T.),
34 phillip.stansfeld@warwick.ac.uk (P.J.S.), fm123@cumc.columbia.edu (F.M.).

35

36 **Keywords:**

37 Lipopolysaccharide, single-particle cryo-electron microscopy, molecular dynamics
38 simulations, structural biology, undecaprenyl pyrophosphate, WaaL ligase, lipid A, O-
39 antigen, membrane proteins, transglycosylation, glycosyltransferase

40

41

42

43

44 **Abstract**

45 **The outer membrane of Gram-negative bacteria has an external leaflet largely**
46 **composed of lipopolysaccharides (LPS), that provides a selective permeation barrier,**
47 **particularly against antimicrobials¹. The final and crucial step in LPS biosynthesis is**
48 **the addition of a species-dependent O-antigen to the lipid A core oligosaccharide,**
49 **catalyzed by the O-antigen ligase WaaL². Here we present structures of WaaL from**
50 ***Cupriavidus metallidurans*, both apo and complexed with its lipid-carrier undecaprenyl**
51 **pyrophosphate, determined by single-particle cryo-electron microscopy to 3.5 Å and 3.2**
52 **Å resolution, respectively. The structures reveal that WaaL is comprised of 12**
53 **transmembrane helices and a predominantly α -helical periplasmic region, which we**
54 **show contains many of the conserved residues required for catalysis. We observe a**
55 **conserved fold within the GT-C family of glycosyltransferases and hypothesize a**
56 **common mechanism for shuttling the undecaprenyl-based carrier to and from the**
57 **active site. The structures, combined with genetic, biochemical, bioinformatics and**
58 **molecular dynamics simulation experiments, provide molecular details on how the**
59 **ligands come in apposition, and allows us to propose a mechanistic model for catalysis.**
60 **Our work presents a structural basis for LPS maturation by a novel member of the GT-**
61 **C superfamily of glycosyltransferases.**

62

63

64 **Main**

65 The external leaflet of the outer membrane of Gram-negative bacteria is comprised
66 mainly of lipopolysaccharides (LPS), making it a robust permeability barrier. LPS is critical
67 for bacterial fitness during infection, can impact pathogenicity, and serves as one of the
68 conserved microorganism-associated molecular patterns recognized by the mammalian innate
69 immune system^{1,3,4}. LPS is comprised of a lipid anchor (termed lipid A), an oligosaccharide
70 (OS) core, and an O-antigen, which is a highly variable polysaccharide composed of
71 repeating sequences of three to six sugar moieties^{3,5,6}. The O-antigen domain of LPS has been
72 shown to contribute to bacterial evasion of complement-mediated killing, impact host
73 autoimmunity through molecular mimicry, and alter bacterial adherence to host tissue⁷⁻⁹.
74 Within *E. coli* alone, more than 187 different O-antigens have been identified¹⁰, and many of
75 the corresponding O-antigen structures have been determined¹¹.

76 The polysaccharide repeats that constitute the O-antigen are synthesised in the
77 bacterial cytoplasm by a series of glycosyltransferases, and then attached to the lipid carrier
78 undecaprenyl pyrophosphate (Und-PP), before being flipped to the periplasmic leaflet of the
79 inner membrane^{3,12}. This occurs via the Wzy polymerase, ABC transporter or the less well-
80 characterized Synthase pathway, according to the composition of the O-antigen and the
81 nature of transport and elongation (**Extended Data Fig. 1a**)¹³. In all cases, the final step is
82 the addition of O-antigen to the lipid A core OS, carried out by the O-antigen ligase WaaL,
83 via a metal-independent glycosyltransferase reaction (**Fig 1a** and **Extended Data Fig. 1b**)^{2,14}.
84 Mutations within the gene encoding for WaaL prevent this ligation step, are devoid of O-
85 antigen and accumulate Und-PP-linked precursors in the periplasm¹⁵. WaaL is predicted to
86 have 12 transmembrane (TM) helices and a significant periplasmic region between TM helix
87 9 and TM helix 10^{5,16,17}, shown to be essential for the formation of mature LPS^{1,7}.

88 To investigate the molecular details of the final assembly step in LPS biosynthesis, we
89 determined structures of WaaL by single-particle cryo-electron microscopy (cryo-EM), in its
90 ligand-bound and apo state. Combining structural information with genetics, biochemical
91 assays, and molecular dynamics (MD) simulations, we provide a rationale for substrate
92 binding as well as a hypothesis for the reaction mechanism.

93 **Structure determination of WaaL**

94 We screened WaaL orthologues from ~200 different species for expression and
95 stability in detergent to select suitable candidates for structural studies. Out of nineteen
96 shortlisted, WaaL from *Cupriavidus metallidurans* (*CmWaaL*; 44kDa) was identified as the
97 most promising. We confirmed that *CmWaaL* is an O-antigen ligase by deleting the gene
98 encoding *CmWaaL* and showing loss of O-antigen ligase activity that could be restored when
99 *CmWaaL* was expressed *in trans* (**Extended Data Fig. 1c**). *CmWaaL* was purified in
100 detergent and reconstituted into lipid-filled nanodiscs for structure determination by cryo-EM
101 (**Extended Data Fig. 1d, e**). In order to overcome current size limitations for this technique
102 and to provide fiducials for particle alignment¹⁸, we screened a synthetic phage display
103 library to select for recombinant antigen-binding fragments (Fabs) against *CmWaaL*¹⁹. Seven
104 high-affinity Fab candidates were screened for complex formation with *CmWaaL*, and
105 WaB10 was chosen due to its high binding affinity (**Extended Data Fig. 1f-h**). Data
106 processing of particles picked from 2378 micrographs allowed us to separate them into two
107 distinct classes resulting in density maps to 3.5 and 3.2 Å resolution (**Extended Data Table 1**
108 and **Extended Data Fig. 2**). We built first into the higher resolution map (**Fig. 1b** and
109 **Extended Data Fig. 3**) residues 5-407 of the 413 amino acids of *CmWaaL*, and then adopted
110 the model to fit the density of the second map.

111 **The structure of Und-PP-bound *CmWaaL***

112 The structure of *CmWaaL* derived from the 3.2 Å map shows a monomer with twelve
113 TM helices and one short cytoplasmic helix (CH) connecting TM helices 2 and 3 (**Fig. 1c, d**).
114 Both the N- and C-termini are on the cytoplasmic side of the membrane. There is also a ~90
115 amino acid region between TM helices 9 and 10 on the periplasmic side which is mainly α -
116 helical, divided into four short α -helical segments (PH 1-4), two of which (PH1 and PH2) are
117 amphipathic and parallel to the membrane (**Fig. 1c, d**). The Fab required for structure
118 determination binds to this periplasmic region (**Fig. 1b** and **Extended Data Fig. 4a, b**).

119 The overall TM core of the protein is tightly packed and comprises TM helices 1-8
120 and 10-12. In contrast, TM helix 9 protrudes from the TM core (**Fig. 1c, d**), and forms a
121 conduit to a central cavity (cavity 1) that is lined with conserved charged and polar residues
122 at the periplasmic surface, and hydrophobic residues within the membrane core (**Fig. 2a,**
123 **Extended Data Fig. 4c** and **Extended Data Fig. 5a-c**). A cluster of four conserved arginines
124 – R139, R191, R242, and R265 – provide a positive net electrostatic charge within this region
125 (**Fig. 2a** and **Extended Data Fig. 5a**). Here, we observed clear non-protein density, which we
126 modeled as two isoprenyl groups and a pyrophosphate, and interpreted it as being a partially
127 ordered Und-PP (**Fig. 2b**). The presence and identity of Und-PP, which co-purified with the
128 protein, was confirmed by thin-layer chromatography (TLC) (**Extended Data Fig. 5d**). R191
129 and R265 coordinate the di-phosphate of Und-PP (**Fig. 2b**) and the polyprenyl tail appears to
130 interact with several conserved hydrophobic residues, including I373, L376, T377 (TM helix
131 11), and V195 (TM helix 8) (**Extended Data Fig. 5e**).

132 The complete Und-PP was modelled by superposition onto the two isoprenyl groups
133 and the pyrophosphate coordinates described above. This WaaL-Und-PP complex was
134 subjected to MD simulations within a lipid membrane. The simulations are consistent with
135 the density map, illustrating that the portion of Und-PP that is visible in the structure is

136 stabilized in the cavity, while the remainder of the undecaprenyl tail is highly mobile within
137 the membrane (**Extended Data Fig. 5f**).

138 To study the effect on enzymatic activity of the four conserved arginines and other
139 potentially functionally important residues in the Und-PP binding cavity, we shifted our
140 attention to *E. coli* (*Ec*) K12, as this organism is more amenable to genetic manipulation and
141 functional characterization. *Ec*WaaL could not be cross-complemented by *Cm*WaaL, likely
142 reflecting differences in chemical composition of the lipid A core OS, which aids in
143 determining WaaL specificity^{5,15}. We therefore generated a homology model of *Ec*WaaL
144 based on the *Cm*WaaL structure, guided by co-evolutionary analysis and the coordinates of a
145 structure modelled by AlphaFold²⁰ (**Extended Data Fig. 6**), and utilized this to select
146 mutants to test functionally in a ligation assay. We observed that the ligase activity is
147 abolished for *Ec*WaaL when R161, R215, R265 and R288 – corresponding to R139, R191,
148 R242 and R265 in *Cm*WaaL – are mutated to alanine (**Extended Data Fig. 7a-c**).

149 We next evaluated the role of these four arginines in *Cm*WaaL ligase activity directly
150 in *Cm*. In this organism, when the WaaL KO was complemented with R191A and R265A *in*
151 *trans*, ligase activity was abolished and almost abolished in R242A, whereas when the
152 Δ waaL was complemented with R139A, activity appeared to be retained (**Fig. 2c** and
153 **Extended Data Fig. 7d**).

154 **The structure of apo *Cm*WaaL**

155 Analysis of the lower (3.5 Å) resolution map showed no evidence of density
156 corresponding to Und-PP (**Extended Data Fig. 8a**), likely representing the apo state of the
157 enzyme. The structure of *Cm*WaaL shows a similar overall fold in both states, with the
158 exception of TM9 (**Extended Data Fig. 8b, c**), which is poorly resolved in the apo state

159 likely due to its flexibility in the absence of Und-PP. R191 and R242 also appear to change
160 conformation (**Fig. 2d**). The density of R265 together with a nearby cluster of conserved
161 histidines (H311, H313 and H383) is weaker, probably because of the more dynamic nature
162 of the apo state (**Extended Data Fig. 8d**).

163 The structures in apo and Und-PP-bound states of *CmWaaL*, coupled to functional
164 experiments, suggest that R191 and R242 (*EcR215* and *EcR265*) might be involved in
165 shuttling the Und-PP in and/or out of its binding pocket. Once the substrate is in place, R191
166 (*EcR215*), together with R265 (*EcR288*) appear to play a dominant role in coordinating it.

167 *CmR139* and the equivalent *EcR161* could instead have different roles in the two
168 orthologues. *CmR139* is in a flexible linker between TM helix 5 and 6, and is the most distant
169 of the four arginine residues from the bound Und-PP. In the model, *EcR161* is directed
170 towards *EcD389*, previously shown to be important for function². *EcD389* likely corresponds
171 to *CmQ378*, which when mutated to alanine does not affect activity (**Extended Data Fig.**
172 **7e**)³, suggesting inter-species differences which may correlate with diversity in chemical
173 composition of LPS.

174 **Putative lipid A-binding site**

175 A second cavity (cavity 2) is located between the first three TM helices and extends
176 over the periplasmic surface of the enzyme to cavity 1 (**Fig. 2a**). We hypothesize that this
177 may be the binding site for lipid A. By performing a focused classification around cavity 2,
178 we identified density consistent with lipid within the proposed lipid A binding site (**Fig. 3a**).
179 In this region of the density map, we also observed a membrane deformation in the
180 periplasmic leaflet adjacent to TM helices 1-3 (**Fig. 3a**). Membrane deformation was also
181 observed in MD simulations, with and without bound lipid A. This appears to be induced by

182 the presence of two short TM helices (1 and 2) in conjunction with the buried basic residues,
183 R28 and R92. In these simulations, the phospholipid head groups deform ~ 8.5 Å towards
184 both arginines to accommodate the hydrophobic mismatch induced by the two short TM
185 helices (**Fig. 3b-d**). The thinning of the membrane could favour the capture of the shorter,
186 C10 to C14, acyl tails of lipid A, in comparison to the longer, inner membrane phospholipid
187 species. This is comparable to the membrane thinning – from 38 to 33 Å thickness – observed
188 around outer membrane proteins when embedded and simulated in a model phospholipid
189 membrane²¹. In addition, the distance between the two arginine CZ atoms, at ~ 8 Å, is ideally
190 positioned to dynamically coordinate the phosphate groups of lipid A, which are ~ 10 Å apart.
191 Furthermore, both residues are also located in the same plane of the membrane.

192 The two short TM helices and the basic residues in *CmWaaL* are also conserved in
193 *EcWaaL* (K45 and K111). However, alanine mutations of these residues in *EcWaaL* did not
194 abolish O-antigen ligation (**Extended Data Fig. 7a-c**), although the *CmWaaL* R92A mutant
195 does show a slight decrease in activity (**Extended Data Fig. 7d, e**), as does the double
196 mutant K45A and K111A in *EcWaaL* (**Extended Data Fig. 7a-c**). Tryptophan mutations on
197 residues at the interface between cavity 1 and cavity 2 were also carried out to monitor their
198 effect on ligase activity. T168W and A394W did not abolish O-antigen ligation, whereas
199 T170W did (**Extended Data Fig. 7a-c and f**). This could be due to the T170W mutant
200 having a steric impact on Und-PP binding (**Extended Data Fig. 7g**). We also expect that the
201 activity of WaaL could partly be retained due to the large size and complexity of lipid A and
202 the nature of the multifaceted binding interface between the lipid A core OS and WaaL.
203 Alternatively, lipid A could bind in cavity 1, near Und-PP (**Extended Data Fig. 7h**), a
204 hypothesis we cannot exclude *a priori*. However, this could result in steric clashes between
205 both substrates. Furthermore, the geometry of the two ligands would likely be somewhat
206 constrained, with the groups to be ligated positioned at an acute angle, when compared with

207 the more linear arrangement observed if the substrates are modelled bound to two distinct
208 sites.

209 **Proposed mechanism of action**

210 The reaction catalyzed by WaaL is known to be independent of ATP and metal ions²,
211 and the energy required to drive it has been suggested to result from cleavage of the bond
212 between the distal phosphate group of Und-PP and its O-antigen cargo²². This is analogous to
213 classical glycosyltransferases in which a nucleotide diphosphate sugar is the substrate²³. In
214 inverting glycosyltransferases, nucleophilic attack by the acceptor hydroxy group leads to an
215 inversion of stereochemistry at the anomeric center of the donor substrate. These enzymes
216 typically use a catalytic base and a bound metal ion that stabilizes the leaving phosphate
217 groups. However, metal ion-independent inverting glycosyltransferases also exist and use
218 basic amino acids such as arginine, lysine, or histidine to perform a similar function to that of
219 the metal ion^{2,16}.

220 We propose a mechanism for *Ec*WaaL in which the absolutely conserved *Ec*H338
221 abstracts a proton from the leading hydroxyl of the terminal outer core of LPS. This would
222 enable the oxygen to perform a nucleophilic attack at the C1 carbon of the Und-PP-linked O-
223 antigen sugar ring and induce cleavage of the sugar-phosphate bond (**Fig. 4a, b**). *Ec*H338
224 appears to be stabilised by a network of hydrogen bonds involving nearby *Ec*H336 and
225 *Ec*E343. The enzyme would then reset as the proton moves from *Ec*H338 to the
226 pyrophosphate of Und-PP. The Und-PP moiety is held in position by *Ec*R215 and *Ec*R288, as
227 detailed above (**Fig. 4b**). The mutation *Ec*H338A abolishes enzymatic activity (**Fig. 4c**), as
228 does mutagenesis of the corresponding residue in *Cm*WaaL, *Cm*H313A (**Extended Data Fig.**
229 **7d, e**). The residues *Ec*H336 and *Ec*E343, which are adjacent to *Ec*H338 in the structure, also
230 significantly reduce overall activity when mutated to alanine. We speculate that they might

231 stabilise the position of *Ec*H338, in order for the mechanism to proceed (**Fig. 4c, d**).
232 Inspection of the structure shows that highly conserved residues *Ec*N339 and *Ec*E340 are also
233 in the vicinity of the active site; however, alanine mutants of these residues showed no
234 change in activity compared to the wild-type enzyme and thus are not included in our
235 proposed mechanism (**Fig. 4c, d**).

236 In addition to MD simulations with bound Und-PP, we also performed MD
237 simulations of the apo enzyme (**Extended Data Fig. 9a**). Based on these experiments, we
238 observed TM helix 9 in two discrete states, which we defined as the closed and the open state
239 (**Extended Data Fig. 9b**). In the absence of Und-PP, an outward movement of TM helix 9 is
240 observed, thereby transitioning from a closed to an open state. This appears to be driven by
241 an electrostatic repulsion of *Cm*R242 (*Ec*R265) from the adjacent basic groups of the active
242 site, in particular *Cm*R191 (*Ec*R215) (**Extended Data Fig. 9b**).

243 **Features of GT-C enzymes that use Und-PP** The structure of WaaL reveals that it
244 shares an overall similar fold as *T. thermophilus* (*Tt*) RodA²⁴, with an C α RMSD of 4.73 Å
245 over 248 residues (**Extended Data Fig. 10a**). RodA is a transglycosylase of the shape,
246 elongation, division and sporulation (SEDS) family of proteins²⁵, critically required for
247 peptidoglycan cell wall formation. Mechanistically, WaaL is a transferase whereas RodA is a
248 processive polymerase. Both utilise Und-PP substrates and appear to share a similar helical
249 structural arrangement with conserved arginines lining the binding pocket. Indeed, R242 in
250 *Cm*WaaL and R203 in *Tt*RodA are both highly conserved and could adopt the same
251 mechanism of shuttling the Und-PP into or out of the active site (**Extended Data Fig. 10b**).
252 The major structural distinction between WaaL and RodA is that the latter lacks the first two
253 TM helices, which we propose are integral to binding the lipid A core OS (**Extended Data**
254 **Fig. 10a**).

255 We also noticed structural and topological similarities between WaaL, PglB and ArnT
256 glycosyltransferases (**Extended Data Fig. 10b**)²⁶⁻²⁸. ArnT catalyzes the transfer of a sugar
257 moiety via a undecaprenyl-phosphate (Und-P) carrier to lipid A²³, while the metal-dependent
258 PglB is a protein glycosyltransferase²⁸. For all three enzymes, residues in the periplasmic
259 loops have been shown to be critical for substrate recognition and catalysis^{2,23,26}, suggesting
260 commonalities in structure, function and mechanism.

261 **Discussion**

262 We have determined the structures of Und-PP bound and apo *Cm*WaaL by cryo-EM,
263 to 3.2 Å and 3.5 Å resolution, respectively. The structure reveals two major cavities on the
264 periplasmic side, which we observe and suggest, respectively, are the binding sites for Und-
265 PP and lipid A. There are conserved residues bridging these two cavities, that have previously
266 been suggested to be involved in the ligation of the O-antigen to the lipid A core OS^{2,5,7,17}.

267 We have combined structural evidence, MD simulations and biochemical experiments
268 to propose a reaction mechanism in which the O-antigen linked Und-PP is shuttled into and
269 coordinated within the binding pocket by a set of conserved arginines. Subsequently, the O-
270 antigen is transferred from the Und-PP onto the lipid A core OS via a reaction carried out by
271 a highly conserved histidine, in turn coordinated by another histidine and a glutamate. WaaL
272 shares features with metal ion-independent inverting glycosyltransferases to bring about
273 catalysis, but utilizes a membrane embedded Und-PP substrate as opposed to the soluble
274 nucleotide diphosphate moiety of classical nucleoside glycosyltransferases^{2,29}. In both cases –
275 Und-PP-linked, or nucleotide diphosphate-linked sugars – the leaving group upon glycosyl
276 transfer is a diphosphate molecule and the proximal sugar to the distal phosphate is O-linked
277 to the terminal sugar of the acceptor^{9,23}.

278 We propose that the lipid A binding site is on the opposite side of the structure from
279 the location of the bound Und-PP. This site is coordinated by two basic residues and is
280 shaped by two unique short TM helices (1 and 2). These helices induce a membrane
281 deformation that appears to draw the phospholipids towards two basic residues, *CmR28* and
282 *CmR92*, that are appropriately spaced to coordinate the phosphate groups of the lipid A
283 moiety of LPS. The distance between this binding site and that of the Und-PP is ~ 25 Å,
284 which is comparable to the dimensions of the core OS of LPS. This suggests that
285 carbohydrates of the immature LPS might rest on the periplasmic surface of WaaL to position
286 the terminal outer core sugar for the attachment of O-antigen.

287 The structure of *CmWaaL* in its Und-PP bound state, along with the previously
288 published structures of RodA-PBP2, PglB and ArnT, has allowed us to identify structural
289 similarities^{24,26,28}. In all these cases, we observe a TM helix protruding from the helical
290 bundle, and a short amphipathic helix parallel to the membrane connecting the protruding
291 helix back to the helical bundle, creating a binding cavity for the ligand (**Extended Data Fig.**
292 **10**)²⁴. This suggests an evolutionary relationship between these enzymes which are all
293 members of the GT-C family of glycosyltransferases²³.

294 The structure of *CmWaaL* provides a framework for understanding how O-antigen
295 ligases perform the final, critical, step in LPS maturation of Gram-negative bacteria and
296 offers a structural basis for designing inhibitors of this process in bacterial cell envelope
297 biosynthesis.

298

299

300

301

302

303 **Main Text References**

304 1 Valvano, M. A. Export of O-specific lipopolysaccharide. *Front. Biosci* **8**, s452-s471
305 (2003).

306 2 Ruan, X., Loyola, D. E., Marolda, C. L., Perez-Donoso, J. M. & Valvano, M. A. The
307 WaaL O-antigen lipopolysaccharide ligase has features in common with metal ion-
308 independent inverting glycosyltransferases. *Glycobiology* **22**, 288-299 (2012).

309 3 Whitfield, C. & Trent, M. S. Biosynthesis and export of bacterial lipopolysaccharides.
310 *Annual review of biochemistry* **83**, 99-128 (2014).

311 4 Woodward, L. & Naismith, J. H. Bacterial polysaccharide synthesis and export.
312 *Current opinion in structural biology* **40**, 81-88 (2016).

313 5 Kaniuk, N. A., Vinogradov, E. & Whitfield, C. Investigation of the Structural
314 Requirements in the Lipopolysaccharide Core Acceptor for Ligation of O Antigens in
315 the Genus Salmonella WAAL “LIGASE” IS NOT THE SOLE DETERMINANT OF
316 ACCEPTOR SPECIFICITY. *Journal of Biological Chemistry* **279**, 36470-36480
317 (2004).

318 6 Raetz, C. R., Reynolds, C. M., Trent, M. S. & Bishop, R. E. Lipid A modification
319 systems in gram-negative bacteria. *Annu. Rev. Biochem.* **76**, 295-329 (2007).

320 7 Hong, Y. & Reeves, P. R. Model for the controlled synthesis of O-antigen repeat units
321 involving the WaaL ligase. *MSphere* **1** (2016).

322 8 Lundstedt, E., Kahne, D. & Ruiz, N. Assembly and Maintenance of Lipids at the
323 Bacterial Outer Membrane. *Chemical Reviews* (2020).

324 9 Whitfield, C., Williams, D. M. & Kelly, S. D. Lipopolysaccharide O-antigens-
325 bacterial glycans made to measure. *Journal of Biological Chemistry*, jbc. (2020).

- 326 10 Liu, B. *et al.* Structure and genetics of Escherichia coli O antigens. *FEMS*
327 *microbiology reviews* **44**, 655-683 (2020).
- 328 11 Feldman, M. F. *et al.* The activity of a putative polyisoprenol-linked sugar translocase
329 (Wzx) involved in Escherichia coli O antigen assembly is independent of the chemical
330 structure of the O repeat. *Journal of Biological Chemistry* **274**, 35129-35138 (1999).
- 331 12 Bertani, B. & Ruiz, N. Function and biogenesis of lipopolysaccharides. *EcoSal Plus* **8**
332 (2018).
- 333 13 Schmid, J., Sieber, V. & Rehm, B. Bacterial exopolysaccharides: biosynthesis
334 pathways and engineering strategies. *Frontiers in microbiology* **6**, 496 (2015).
- 335 14 Ruan, X. & Valvano, M. A. In vitro O-antigen ligase assay. In *Glycosyltransferases*
336 185-197 (Springer, 2013).
- 337 15 Abeyrathne, P. D., Daniels, C., Poon, K. K., Matewish, M. J. & Lam, J. S. Functional
338 characterization of WaaL, a ligase associated with linking O-antigen polysaccharide
339 to the core of Pseudomonas aeruginosa lipopolysaccharide. *Journal of bacteriology*
340 **187**, 3002-3012 (2005).
- 341 16 Pérez, J. M., McGarry, M. A., Marolda, C. L. & Valvano, M. A. Functional analysis
342 of the large periplasmic loop of the Escherichia coli K- 12 WaaL O- antigen ligase.
343 *Molecular microbiology* **70**, 1424-1440 (2008).
- 344 17 Islam, S. T., Taylor, V. L., Qi, M. & Lam, J. S. Membrane topology mapping of the
345 O-antigen flippase (Wzx), polymerase (Wzy), and ligase (WaaL) from Pseudomonas
346 aeruginosa PAO1 reveals novel domain architectures. *MBio* **1**, e00189-00110 (2010).
- 347 18 Nygaard, R., Kim, J. & Mancina, F. Cryo-electron microscopy analysis of small
348 membrane proteins. *Current Opinion in Structural Biology* **64**, 26-33 (2020).
- 349 19 Dominik, P. K. & Kossiakoff, A. A. in *Methods in enzymology* Vol. 557 219-245
350 (Elsevier, 2015).

- 351 20 Jumper, J. *et al.* Highly accurate protein structure prediction with AlphaFold. *Nature*
352 **596**, 583-589 (2021).
- 353 21 Newport, T. D., Sansom, M. S. P. & Stansfeld, P. J. The MemProtMD database: a
354 resource for membrane-embedded protein structures and their lipid interactions.
355 *Nucleic acids research* **47**, D390-D397 (2019).
- 356 22 Lazarus, M. B., Nam, Y., Jiang, J., Sliz, P. & Walker, S. Structure of human O-
357 GlcNAc transferase and its complex with a peptide substrate. *Nature* **469**, 564-567
358 (2011).
- 359 23 Valvano, M. A. Glycan translational reactions in the periplasmic space. in *Recent*
360 *Trends in Carbohydrate Chemistry* 37-49 (Elsevier, 2020).
- 361 24 Sjodt, M. *et al.* Structural coordination of polymerization and crosslinking by a
362 SEDS–bPBP peptidoglycan synthase complex. *Nature Microbiology* **5**, 813-820
363 (2020).
- 364 25 Meeske, A. J. *et al.* SEDS proteins are a widespread family of bacterial cell wall
365 polymerases. *Nature* **537**, 634-638 (2016).
- 366 26 Petrou, V. I. *et al.* Structures of aminoarabinose transferase ArnT suggest a molecular
367 basis for lipid A glycosylation. *Science* **351**, 608-612 (2016).
- 368 27 Tavares-Carreón, F., Fathy Mohamed, Y., Andrade, A. & Valvano, M. A. ArnT
369 proteins that catalyze the glycosylation of lipopolysaccharide share common features
370 with bacterial N-oligosaccharyltransferases. *Glycobiology* **26**, 286-300 (2016).
- 371 28 Napiórkowska, M. *et al.* Molecular basis of lipid-linked oligosaccharide recognition
372 and processing by bacterial oligosaccharyltransferase. *Nature structural & molecular*
373 *biology* **24**, 1100-1106 (2017).
- 374 29 Ruan, X., Monjarás Feria, J., Hamad, M. & Valvano, M. A. Escherichia coli and
375 Pseudomonas aeruginosa lipopolysaccharide O- antigen ligases share similar

376 membrane topology and biochemical properties. *Molecular microbiology* **110**, 95-113
377 (2018).
378 30 Voss, N. R. & Gerstein, M. 3V: cavity, channel and cleft volume calculator and
379 extractor. *Nucleic acids research* **38**, W555-W562 (2010).

380

381 **Main Text Figure Legends**

382 **Figure 1 | The central role of WaaL in lipopolysaccharide biosynthesis in bacteria and**
383 **the structure of *CmWaaL*.** **a**, Atomic representation of a *OI* O-antigen ligation to the *RI*
384 lipid A core OS. The O-antigen is transferred to the lipid A core OS by WaaL, forming the
385 mature LPS. After ligation, Und-PP is recycled. **b**, Cryo-EM density map of the Und-PP
386 bound *CmWaaL*-Fab complex. Density corresponding to the variable region of the Fab
387 (vFAB) is shown in grey and *CmWaaL* in rainbow color. Representation is in rainbow color
388 from the N-terminus (blue) to the C-terminus (red). **c**, Schematic diagram showing the
389 topology of WaaL, consisting of 12 TM helices and a large periplasmic loop between TM
390 helix 9 and 10. **d**, The 3.2 Å cryo-EM structure of Und-PP bound WaaL shown in two
391 different orientations, with the 12 TM helices colored as in **e**. The N- and C- termini are
392 labeled. The right-hand side shows a 90° rotation with helices numbered, as viewed from the
393 top. Und-PP is shown as sticks (in gold). Approximate membrane boundaries are represented
394 with dotted lines.

395

396 **Figure 2 | Significant structural features of *CmWaaL*.** **a**, Cavities within the *CmWaaL*
397 structure. *CmWaaL* is shown in ribbon representation in grey, and the two cavities as a semi-
398 transparent surface, with cavity 1 in green and cavity 2 in blue. Volumes were calculated
399 using the Voss Volume Voxelator (3V) server³⁰, using probes with 10 and 2 Å radii,

400 corresponding to the outer and inner probe, respectively. The approximate membrane
401 boundaries are represented with dotted lines. Und-PP (in gold) and the key arginine (R191,
402 R242, R265) residues for *CmWaaL* are shown as sticks. **b**, Close up view of R191 and R265
403 coordinating the Und-PP (in gold) within the binding pocket. The cryo-EM density assigned
404 to bound Und-PP is displayed as a semi-transparent grey mesh. **c**, Functional analysis of
405 *CmWaaL* ligase activity in whole cells. LPS gel showing O-antigen extension in *C.*
406 *metallidurans* expressing *CmWaaL* variants (mutated *CmWaaL* residues denoted in blue). Ø
407 indicates empty plasmid. **d**, Close-up view of the Und-PP binding pocket in the apo structure
408 (pink) and the Und-PP bound (grey), superimposed, showing R139, R191, R242 and R265 in
409 sticks with CPK coloring.

410

411 **Figure 3 | A putative binding site for lipid A.** **a**, Cryo-EM density of WaaL (grey)
412 incorporated into a nanodisc (salmon), showing a slice through the nanodisc where
413 membrane deformation can be observed and outlined with a dashed blue box. Also, in salmon
414 a lipid tail density is seen in the putative lipid A binding site. The density for the Fab is not
415 included. **b**, The mean phosphate atom positions, highlighting a strong thinning of the
416 membrane of ~ 8.5 Å around the two short helices (TM helix 1 and 2) in the apo *CmWaaL*
417 MD simulations. The mean phosphate position is coloured according to the deviation from
418 the mean (blue = outward, red = inward). **c**, Contact of lipid A phosphates to *CmWaaL* in
419 MD simulation. Throughout the MD simulations, the phosphates of lipid A remain in contact
420 with R28 and to a lesser extent with R92 and Q384. The residue contacts with threshold
421 above 0.5 are shown as sticks. **d**, Left, top view of *CmWaaL*, in ribbon, highlighting
422 conserved residues, shown in sticks. Distance between R28 and R92 and between the
423 phosphates of lipid A core and the Und-PP are shown as black lines. Right, lipid A chemical
424 structure, with distances marked as black lines.

425

426 **Figure 4 | Mechanism of catalysis for WaaL. a,** Schematic representation of the ligation of
427 the O-antigen linked Und-PP to the lipid A core OS in *EcWaaL*, viewed from the periplasmic
428 side of the membrane. In all cases, key arginine (R161, R215, R265, R288) and histidines
429 (H338, H336) are shown as grey sticks. Left panel shows a surface representation for both
430 lipid A (peach) with its inner (cyan) and outer (purple) core OS and the O-antigen (green)
431 linked Und-PP (yellow) approaching their binding sites on the apo-state of WaaL. Middle
432 panel shows the coordination of both O-antigen linked Und-PP and lipid A core OS in both
433 sites. Right panel shows the mature LPS, with the Und-PP (yellow) product still bound, as
434 shown in the cryo-EM structure. **b,** Residues within the active site of *EcWaaL* are shown
435 around the Und-PP-linked *OI* O-antigen N-acetylglucosamine and terminal *RI* outer core
436 glucose. H338 (highlighted in green) is coordinated by a H-bond network between H336 and
437 E343, which permits the abstraction of a proton from the terminal hydroxyl of the *RI* outer
438 core glucose to protonate H338. The deprotonated oxygen may then perform a nucleophilic
439 attack on the *CI* of the *OI* N-acetylglucosamine. This allows cleavage of the GlcNAc-
440 phosphate bond. To reset the enzyme, H338 will deprotonate, with the proton possibly
441 transferring to the phosphate of Und-PP, which then leaves the active site. **c,** Functional
442 analysis of *EcWaaL* ligase variants in whole cells by LPS gel analysis. WaaL proteins were
443 expressed from plasmid pWSK29 in the W3110 $\Delta waaL$ strain. \emptyset indicates empty plasmid. **d,**
444 Key residues involved in the putative ligation mechanism and ligand coordination within
445 *EcWaaL*. The *EcWaaL* homology model is based on the *CmWaaL* structure and shown as
446 cartoon. Key residues R215, R265, R288, E343, H336, H338, and D389 are shown as sticks.

447

448

449

450
451
452
453
454
455
456
457
458
459
460
461
462
463
464
465
466
467
468
469
470
471
472
473

Methods

Target identification and cloning. Nineteen putative WaaL genes corresponding to a wide genomic background were identified based on a bioinformatics approach, as previously described³¹. Ligation independent cloning (LIC) was used to clone these nineteen orthologues into five different LIC-adapted expression vectors (pNYCOMPS-Nterm, pNYCOMPS-Cterm, pMCSG7, pNYCOMPS-N23 and pNYCOMPS-C23), all bearing protease-cleavable decahistidine tags for metal-affinity chromatography-based purification. Small scale expression and purification tests were performed as previously described³², to identify eleven unique targets as “expression positive” from the small-scale expression tests. These eleven candidates were carried forward for midscale expression, purification and detergent screens as previously described³², for the selection of *Cupriavidus metallidurans* (*Cm*) as the best candidate (protein accession code: WP_011517284.1). All cloning and initial protein characterization were performed at the protein production core facility of the former New York Consortium on Membrane Protein Structure (NYCOMPS)³³, now the Center on Membrane Protein Production and Analysis (COMPPA).

474 **Protein expression and purification in detergent.** WaaL from *Cupriavidus metallidurans*
475 (*CmWaaL*), cloned in the pNYCOMPS-Cterm vector, was used to transform
476 BL21(DE3)pLysS *E. coli* competent cells, and grown overnight in 2xYT medium
477 supplemented with 100 µg/mL ampicillin and 35 µg/mL chloramphenicol at 37°C with
478 shaking (240 r.p.m.). The next day, 800 mL (large scale for protein expression) or 8 mL
479 (small scale to test expression) of the same medium were inoculated with the starter culture at
480 1:100 ratio, and left to grow at 37°C with shaking (240 r.p.m.), until OD600 reached 0.8-1.2.
481 Temperature was then reduced to 22°C, protein expression was induced with 0.2 mM
482 isopropyl β-D-1-thiogalactopyranoside (IPTG), and the culture was incubated overnight with
483 shaking (240 r.p.m.). Cells were harvested by centrifugation (3,700 r.p.m. for 15 min) at 4°C,
484 washed once with phosphate buffered saline (PBS) and centrifuged again to produce a solid
485 pellet that was stored at -80°C, until further use. For large-scale purification of *CmWaaL*, cell
486 pellets were resuspended in lysis buffer containing 20 mM HEPES pH 7.5, 200 mM NaCl, 20
487 mM MgSO₄, 10 µg/mL Dnase I, 8 µg/mL Rnase A, 1 mM tris(2-carboxyethyl)phosphine
488 hydrochloride (TCEP), 1 mM PMSF, and Complete Mini EDTA-free protease inhibitor
489 cocktail (Roche) used according to the manufacturer's instructions. Cells were lysed with an
490 Emulsiflex C3 homogenizer (Avestin) and the lysate was solubilized for 2 hours with *n*-
491 dodecyl-β-D-maltopyranoside (DDM; Anatrace) added to a final concentration of 1% (w/v),
492 in a volume of approximately 40 mL per cell pellet from 800 mL culture. Insoluble material
493 was removed by ultracentrifugation at 34,000 r.p.m. for 30 min at 4°C and the protein was
494 purified from the supernatant by metal-affinity chromatography using Ni-NTA agarose beads
495 (Qiagen). The supernatant after addition of 40mM imidazole was incubated with pre-
496 equilibrated Ni-NTA agarose beads (0.7 mL per pellet from an 800 mL culture) overnight.
497 The beads were then loaded on a column and washed with 10 column volumes of 20 mM
498 HEPES pH 7.5, 500 mM NaCl, 75 mM imidazole and 0.03% (w/v) DDM. Protein was eluted

499 with 4 column volumes of 20 mM HEPES pH 7.0, 150 mM NaCl, 300 mM Imidazole, and
500 0.03% (w/v) DDM. Imidazole was removed from the eluted protein by exchanging buffer to
501 20 mM HEPES pH 7.0, 200 mM NaCl, 0.03% (w/v) DDM (final protein buffer) using a PD-
502 10 desalting column (GE Healthcare).

503 **Nanodisc incorporation after detergent purification.** The imidazole-containing buffer of
504 the protein eluted from metal-affinity chromatography was desalted using a PD-10 column
505 into the final protein buffer. *CmWaaL* was incorporated into lipid nanodiscs with a 1:300:5
506 molar ratio of protein:1-palmitoyl-2-oleoyl-sn-glycero-3-phospho-(1'-rac-glycerol) (POPG):
507 membrane scaffold protein 1E3D1 (MSP1E3D1)^{34,35}. This mixture was incubated at 4°C for
508 2 h with gentle agitation. Reconstitution was initiated by removing detergent with the
509 addition of Bio-beads (Bio-Rad) at 4°C overnight with constant rotation. Bio-beads were
510 removed and the nanodisc reconstitution mixture was bound again to Ni²⁺-NTA resin at 4°C
511 for 2 h to remove empty nanodiscs. The resin was washed with 10 column volumes of wash
512 buffer (20 mM HEPES pH 7.5, 150 mM NaCl, and 60 mM imidazole) followed by four
513 column volumes of elution buffer (20 mM HEPES pH 7.0, 150 mM NaCl, and 300 mM
514 imidazole). Subsequently, the protein was incubated with TEV protease³⁶ to cleave the
515 decahistidine tag (~0.5 mg TEV protease added per pellet equivalent from 800 mL of initial
516 bacterial culture) overnight at 4°C, while exchanging into an imidazole free buffer using a
517 3.5K cut-off Slide-A-Lyzer Dialysis Cassettes (Thermofisher). The sample was then passed
518 through a column containing Ni²⁺-NTA beads to separate the cleaved decahistidine tag, the
519 TEV protease and uncleaved protein. The cleaved protein was further purified by loading
520 onto a Superdex 200 Increase 10/300 GL size-exclusion column (GE Healthcare Life
521 Sciences) in gel filtration buffer (20 mM HEPES pH 7.0 and 150 mM NaCl). Protein
522 typically eluted as a sharp monodispersed peak, observed by monitoring absorbance at 280
523 nm (**Extended Data Fig. 1d**).

524 **Phage display to identify *CmWaaL*-specific Fab fragments (WaB10).** *CmWaaL* was
525 reconstituted into nanodiscs formed using chemically biotinylated MSP1E3D1, which were
526 prepared as previously described¹⁹. Biotinylation efficiency was evaluated by a pull-down
527 assay using streptavidin-coated paramagnetic particles (Promega). Phage displayed synthetic
528 antigen binder (sAB) Library E^{37,38} (kindly prepared by S. Mukherjee) was used as the naïve
529 starting pool. Library E and the target were both diluted into selection buffer (20 mM Hepes,
530 pH 7.4, 200 mM NaCl, 1% BSA) and selections were performed using a protocol adapted
531 from prior publications^{39,40}. In round one, biopanning was performed manually using 300 nM
532 of *CmWaaL* immobilized onto magnetic beads. Following a one-hour incubation, beads were
533 washed three times with selection buffer and then used to subsequently infect log-phase *E.*
534 *coli* XL-1 Blue cells. Infected cells were used to inoculate 30 mL cultures containing
535 ampicillin (100 µg/mL) and M13-K07 helper phage (10⁹ pfu/mL), and phage were amplified
536 overnight. Four additional rounds of biopanning were performed by stepwise reduction of the
537 target concentration to increase the stringency of selection. Rounds 2-5 were performed semi-
538 automatically using a Kingfisher Beads Handling Robot (Thermo), and phage from each
539 preceding round were amplified and used as the input pools. In addition, the amplified phage
540 pool was pre-cleared using 200 µL of streptavidin beads, and in all rounds 1.5 µM of empty
541 MSP1E3D1 nanodiscs were used as competitors in solution. Finally, in the last four rounds,
542 phage were eluted from magnetic beads using a 15 min incubation with 1% Fos-choline 12
543 (Anatrace).

544 **Single-point phage ELISA.** *E. coli* XL-1 Blue cells were infected with phage from the 4th
545 and 5th round pools and plated on LB-agar supplemented with 100 µg/mL ampicillin. The
546 following day, individual colonies harboring phagemids were used to inoculate 400 µL of
547 2xYT media supplemented with ampicillin (100 µg/mL) and M13-K07 helper phage (10⁹
548 pfu/mL). Phage were amplified overnight with shaking (280 r.p.m.). Single-point phage

549 ELISA was subsequently performed as previously described (**Supplementary Table 1**)^{39,40}.
550 All amplified phage were tested against *CmWaaL* in MSP1E3D1 nanodiscs (30 nM), empty
551 1E3D1 nanodiscs (50 nM), or buffer alone to determine specific target binding. Bound phage
552 particles were detected by a colorimetric assay using an HRP-conjugated anti-M13
553 monoclonal antibody (GE Healthcare). Binders with high target and low non-specific signal
554 were chosen for subsequent experiments.

555 **sAB cloning, expression, and purification.** All specific binders were sequenced and then
556 cloned into the sAB expression vector RH2.2 (kindly gifted by Sachdev Sidhu) as previously
557 described⁴⁰. All phage and expression vector subclones were sequence-verified at the
558 University of Chicago Comprehensive Cancer Center DNA sequencing facility. sABs were
559 expressed and purified as previously described⁴⁰ and subsequently dialyzed overnight in
560 buffer with 20 mM Hepes, pH 7.5, 150 mM NaCl.

561 **Multi-point sAB ELISA.** To estimate apparent binding affinity of each sAB, multi-point
562 ELISA was performed in triplicate as previously described^{39,40} for each unique sAB. All
563 sABs were again verified for specific binding by testing against *CmWaaL* in MSP1E3D1
564 nanodiscs (30 nM), empty MSP1E3D1 nanodiscs (50 nM), or buffer alone. The amount of
565 bound sAB was measured by a colorimetric assay using an HRP-conjugated anti-Fab
566 monoclonal antibody (Jackson ImmunoResearch). Measured absorbance (A_{450}) values were
567 plotted against the log sAB concentration, and estimated binding affinities (EC_{50}) were
568 determined using a variable slope model with sigmoidal dose response in Prism (GraphPad
569 software) (**Supplementary Table 1**).

570 ***CmWaaL* complex formation with the Fab WaB10.** TEV cleaved *CmWaaL* incorporated
571 into nanodiscs was incubated with the WaB10 Fab on ice for 1 h in a 1:2 molar ratio of

572 protein to Fab. The *CmWaaL*-Fab complex was concentrated and filtered, and then loaded on
573 a Superdex 200 Increase 10/300 GL size-exclusion column in gel filtration buffer (20 mM
574 HEPES pH 7.0 and 150 mM NaCl).

575 **Single-particle cryo-EM vitrification and data acquisition.** Purified *CmWaaL*-Fab
576 complex was concentrated to 1.2 mg/ml using a 50-kDa concentrator (Amicon). 3 μ l of
577 sample was added to a plasma-cleaned (Gatan Solarus) 1.2/1.3 μ m holey gold grid
578 (Quantifoil UltrAuFoil) and blotted using filter paper on one side for 3.5 s using the Vitrobot
579 (Thermofisher) with a blot force of 3 and a wait time of 30 sec, before plunging immediately
580 into liquid ethane for vitrification. The plunger was operating at 4°C with >90% humidity to
581 minimize evaporation and sample degradation. Images were recorded using a Titan Krios
582 electron microscope (FEI), at the Simons Electron Microscopy Center, equipped with an
583 energy filter and a K2 direct electron detector (Gatan K3-BioQuantum) using a 1.061Å pixel
584 size. An energy filter slit width of 20 eV was used during the collection and was aligned
585 automatically every hour using Legimon⁴¹. Data collection was performed using a dose of
586 ~ 70.15 e⁻/Å² across 50 frames (200 ms per frame) at a dose rate of ~ 7.0 e⁻/pix/s, using a set
587 defocus range of -1.3 μ m to -2.8 μ m. A 100 μ m objective aperture was used. In total, 2,378
588 micrographs were recorded over a single two-day collection using an image beam shift data
589 collection strategy. Ice thickness was monitored after every 4th exposure using the Legimon
590 zero-loss peak (ZLP) algorithm and was determined to be 23.1 ± 9.1 nm (SD).

591 **Data processing.** Contrast transfer function (CTF) estimation was performed using Patch
592 CTF as implemented in cryoSPARC v.2.8. Blob picker in cryoSPARC v.2.8 were used to
593 pick particles and inspect picks was used to curate the picks. This resulted in 844,438
594 particles which were then subjected to 2D classification in cryoSPARC v.2.8. 132,664
595 particles were selected for further processing from 2D classes with well-defined high-

596 resolution features. One round of *ab initio* reconstruction was performed in cryoSPARC v.2.8
597 using four classes, with a maximum resolution set at 7 Å and an initial resolution at 9 Å, the
598 best class was selected resulting in a stack of 46,362 particles. Heterogeneous refinement was
599 carried out on this particle stack, after which this stack was then extracted with a 320 pixel
600 size box. This particle stack was subjected to non-uniform refinement in cryoSPARC v.2.8
601 resulting in a 3.9 Å reconstruction. Using a mask covering *CmWaaL* and the variable region
602 of the Fab, local refinement using non-uniform regularization was performed in cryoSPARC
603 v.3.2, resulting in a 3.2 Å density map (**Extended data Fig. 2a**).

604

605 On initial observation it was hypothesized that the particles resulting in the 46,362 particle
606 stack had a mixed population of bound and unbound WaaL particles contributing to this
607 stack, which was mainly due to the density that we attributed to the geranyl diphosphate part
608 of the Und-PP and the density for TM9. We observed that depending on the particles that
609 were selected from the initial 132,664 particles the density of the Und-PP and TM9 had either
610 weak or strong density, indicating that a mixed population of Und-PP bound and unbound
611 may be present within the 132,664 particle stack. To address this, 3D classification was then
612 performed using the initial 132,664 particles, which were extracted with a 400 pixel box size
613 for further processing. These extracted particles were then imported into Relion v3.1.1 for 3D
614 classification using a mask that only included TM9-11 as well as PH1-4, helices that
615 surrounded the Und-PP. In total six classes were obtained, with the initial low pass set at 20
616 Å and the T value set at 40, the two best classes were then selected resulting in a stack of
617 39,844 and 30,514 particles. Both particle stacks were imported back into cryoSPARC v.3.2
618 and using a mask covering *CmWaaL* and the variable region of the Fab for the 39,844
619 particle stack, and a mask covering *CmWaaL* for the 30,514 particle stack, local refinement
620 using non-uniform regularization was performed, resulting in a 3.23 Å density map for the

621 39,844 particle stack and 3.5 Å density map for the 30,514 particle stack (**Extended data**
622 **Fig. 2a**).

623 A 3D classification followed by a focused refinement was performed to obtain the lipid
624 density in our proposed lipid A binding site (**Fig. 3a**). The initial 132,664 particles, which
625 were extracted with a 400 pixel size box were imported into Relion v3.1.1 for 3D
626 classification using a mask surrounding the proposed lipid A site, including residues 29-79
627 and 315-352. In total six classes were obtained, with the initial low pass set at 20 Å and the T
628 value set at 40, the best class containing 50,857 particles was selected. The particle stack was
629 imported into cryoSPARC v.3.2 and using a mask covering *CmWaaL* and the variable region
630 of the Fab a local refinement using non-uniform regularization was performed, resulting in a
631 density map at 3.22 Å resolution that has a clear lipid tail density within the binding cleft of
632 cavity 2 (**Fig. 3a**).

633 **Structural model building and refinement.** To build the *CmWaaL* model, Coot was used
634 for manual model building. We observed extra density within the map of the 39,844 particle
635 stack and were able to fit two isoprenyl groups and a pyrophosphate for the Und-PP
636 (Pubchem ID 5280604) into the density. The map obtained from the 39,844 stack was the
637 local refinement with the *CmWaaL* and the variable region of the Fab (vFAB) mask created
638 that gave the 3.23 Å map that was used to build the backbone and majority of the sidechains.
639 The map from the 30,514 particle stack was a local refinement map created from the
640 *CmWaaL* mask that yielded the 3.5 Å map. *CmWaaL* was modeled *de novo* in Coot using
641 secondary structure predictions from the XtalPred server⁴² as a guide. Subsequent model
642 refinement and adjustment was performed in Coot⁴³⁻⁴⁵ and Phenix^{46,47} iteratively.

643 **Model analysis.** A cavity search using the Solvent Extractor from Voss Volume Voxelator
644 server³⁰ was performed using an outer-probe radius of 10 Angstrom and inner-probe radius of
645 2 Angstrom. Chimera⁴⁸ and ChimeraX⁴⁹ were used to visualize the structures in the figures.

646 **Mutagenesis.** Mutations of the *E. coli* K12 *EcWaaL* (protein accession code:
647 WP_001395405.1), in pWSK29 vector, were generated with an in-house method using KOD
648 polymerase and custom primers.

649 **Expression test of *E. coli* K12 *EcWaaL* mutants.** WaaL (WT and all mutants) from *E. coli*
650 K12 (*EcWaaL*), cloned in the pWSK29 vector, were used to transform BL21(DE3)pLysS *E.*
651 *coli* competent cells, and grown overnight in 2xYT medium supplemented with 100 µg/mL
652 ampicillin and 35 µg/mL chloramphenicol at 37°C with shaking (240 r.p.m.). The next day,
653 50 mL of the same medium were inoculated with the starter culture at 1:100 ratio, and left to
654 grow at 37°C with shaking (240 r.p.m.), until OD600 reached 0.8-1.2. Temperature was then
655 reduced to 22°C, protein expression was induced with 0.2 mM isopropyl β-D-1-
656 thiogalactopyranoside (IPTG), and the culture was incubated overnight with shaking (240
657 r.p.m.). Cells were harvested by centrifugation (3,700 r.p.m. for 15 min) at 4°C, washed once
658 with phosphate buffered saline (PBS) and centrifuged again to produce a solid pellet. Cell
659 pellets were resuspended in 2 ml lysis buffer containing 20 mM HEPES pH 7.5, 200 mM
660 NaCl, 20 mM MgSO₄, 10 µg/mL Dnase I, 8 µg/mL Rnase A, 1 mM tris (2-
661 carboxyethyl)phosphine hydrochloride (TCEP), 1 mM PMSF, and Complete Mini EDTA-
662 free protease inhibitor cocktail (Roche) used according to the manufacturer's instructions.
663 Cells were lysed by sonication and the lysate was solubilized for two hours with DDM, added
664 to a final concentration of 1% (w/v). The solubilized material was clarified by centrifugation
665 for 30 min (13,000 r.p.m.) at 4 °C, and the supernatant was mixed with Ni-NTA agarose
666 beads (Qiagen) and binding allowed to proceed overnight in the presence of 40mM

667 imidazole. The beads were then loaded on a column and washed with five column volumes of
668 20 mM HEPES pH 7.5, 500 mM NaCl, 75 mM imidazole and 0.03% (w/v) DDM. Protein
669 was eluted with two column volumes of 20 mM HEPES pH 7.0, 150 mM NaCl, 300 mM
670 imidazole, and 0.03% (w/v) DDM (100 μ L). Imidazole was removed from the eluted protein
671 by exchanging buffer to 20 mM HEPES pH 7.0, 200 mM NaCl, 0.03% (w/v) DDM by
672 concentrating the protein (Amicon Ultra 0.5 mL; 50 Kda cut-off) and washing the sample
673 through with 5 column volumes of buffer (500 μ L), and repeating this 5 times, until the final
674 step where the samples were concentrated to 20 μ L. The eluates were then separated on a
675 14% SDS-PAGE gel, to confirm expression (**Extended Data Fig. 7c**).

676 **Preparation of Und-PP ($C_{55}H_{101}N_3O_7P_2$)**. The procedure was modified from Danilov *et al.*
677 (1989)⁵⁰. Prenol composed of 11 isoprenoid units ($C_{55}H_{90}O$) and trichloroacetonitrile was
678 dissolved in dichloromethane and added to tetra-n-butylammonium dihydrogen phosphate
679 and the mixture was stirred for 90 min at room temperature. The solvent was evaporated, and
680 the residue was dissolved in tetrahydrofuran. An ammonia solution (25%) was added to the
681 mixture to precipitate the inorganic phosphate, and left overnight at 4⁰ C. The following day,
682 the supernatant was removed, and the pellet was washed twice with tetrahydrofuran. The
683 tetrahydrofuran extracts were pooled and evaporated. The residue was dissolved in a
684 chloroform:methanol mixture (2:1 v/v) and applied onto a DEAE-Sephadex A-25 (acetal
685 form) column. Any unreacted undecaprenol was eluted with a chloroform:methanol mixture
686 (2:1 v/v). The final product was eluted with increasing concentrations of ammonium acetal
687 (0-55 mM). Fractions containing Und-PP were collected and analysed by thin-layer
688 chromatography TLC. The solvent was then evaporated, and the residues were dissolved in a
689 mixture of chloroform:methanol (2:1 v/v) with the addition of a 3% ammonia solution. The
690 Und-PP was stored at -20⁰ C until further use.

691 **Thin-layer chromatography analysis of Und-PP.** TLC analysis was utilized to identify the
692 ligand, as mass spectrometry was not successful. Lipids were extracted from detergent
693 purified *CmWaaL* by adding chloroform:methanol (2:1) in a 1:1 ratio. The solvent for the
694 mobile phase of the TLC on silica gel plates (Millipore; TLC Silica gel 60 F₂₅₄) was a
695 solution of chloroform, methanol and water (65:25:4 per volume ratio). TLC plates were
696 dried for five minutes and placed in an enclosed container along with iodine crystals for
697 staining.

698 **CRISPR-Cas9 gene editing in *Cupriavidus metallidurans*.** To allow for efficient genetic
699 manipulation in *Cupriavidus metallidurans* we adapted our recently optimised single
700 plasmid CRISPR-Cas9 / lambda red recombineering system⁵¹⁻⁵⁷. We utilised a pBBR1MCS2
701 origin of replication, *Streptococcus cas9* controlled by an araBAD promoter; a guide RNA
702 specific to the *CmWaaL* gene controlled by a pTAC promoter for constitutive expression, a
703 764 base pair (bp) area of homology to *WaaL*, the lambda red recombineering genes to
704 improve the efficiency of homologous recombination, and an ampicillin resistance
705 cassette^{54,58,59}. For the knock-out, we first analysed the WT *CmWaaL* sequence via the
706 CRISPR direct website to identify an appropriate N20 sequence, which was incorporated into
707 *CmWaaL* sgRNA. The homology was engineered to contain a 183 bp deletion surrounding
708 the cas9 cut site. The *CmWaaL* specific sgRNA and homology cassettes were cloned into the
709 pBBR1_CRISPR vector. The sequence confirmed plasmid was inserted into the CH34
710 *Cupriavidus metallidurans* isolate via electroporation and appropriate transformants were
711 identified through colony PCR. Transformants were grown at 30°C under ampicillin selection
712 in tryptic soy broth (TSB) and induced with 0.2% arabinose after two hours. Following 12-24
713 hours of induction, the cultures were diluted 1:100 and plated on tryptic soy agar (TSA) +
714 ampicillin at 100 mg/mL and 0.2% arabinose. Appropriate mutants were identified by colony

715 PCR and Sanger sequencing (Genewiz). Mutants were cured of the CRISPR plasmid with
716 serial passage on non-selective media TSA.

717 **Expression test of *CmWaaL* WT and Mutants.** WT and mutant *CmWaaL*, which was
718 cured of the CRISPR plasmid and transformed with pBBR1_WaaL complementation
719 plasmids – all bearing a C-terminal FLAG tag fused to *CmWaaL* WT and mutant constructs
720 for detection purposes – were grown in 5 mL of TSB for 3-4 days and supplemented with 100
721 µg/mL tetracycline at 30°C while shaking (80 r.p.m.). The next day, 50 mL of the same
722 medium were inoculated with the starter culture at 1:100 ratio, and left to grow at 30°C with
723 shaking (80 r.p.m.), for 3-4 days. Cells were harvested by centrifugation (3,700 r.p.m. for 15
724 min) at 4°C to produce a solid pellet. Cell pellets were resuspended in 2 ml lysis buffer
725 containing 20 mM HEPES pH 7.5, 200 mM NaCl, 20 mM MgSO₄, 10 µg/mL Dnase I, 8
726 µg/mL Rnase A, 1 mM TCEP, 1 mM PMSF, and Complete Mini EDTA-free protease
727 inhibitor cocktail (Roche) according to the manufacturer's instructions. Cells were lysed
728 using a sonicator and the lysate was solubilized for two hours with DDM added to a final
729 concentration of 1% (w/v). The solubilized material was then spun on a tabletop centrifuge
730 for 30 min (13,000 r.p.m.) and a portion of the supernatant was loaded on to a 14% SDS-
731 PAGE gel. Protein expression was confirmed by western blot analysis (**Extended Data Fig.**
732 **7d**). Proteins from SDS-PAGE gels were transferred electrophoretically onto nitrocellulose
733 membrane overnight at 200 mA. The membrane was blocked for one hour with 5% BSA and
734 immobilized proteins were probed with an anti-Flag mouse antibody (Sigma's Anti-FLAG®
735 M2 Antibody: #8146)) used at 1:5000 dilution. Immobilized protein:FLAG antibody
736 complexes were detected using a secondary IR-labelled, goat anti-mouse green antibody
737 (IRDye 800CW secondary antibodies: #926-32210) diluted 1:10,000. The immunoblot was
738 developed and quantified using an Odyssey system (LI-COR Biosciences, Lincoln, NE)
739 (**Extended Data Fig. 7d**).

740 **Functional analysis of WaaL variants by LPS gel.** The *Ec* W3110 $\Delta waaL$ mutant was
741 generated by P1 *vir* phage transduction⁶⁰ using the *waaL::km* mutant from the Keio
742 collection⁶¹ and the strain confirmed by PCR. *Ec* cells were grown in lysogeny broth (LB)
743 broth at 37°C and *Cm* in tryptic soy (TB) broth at 30°C supplemented with antibiotics. Cells
744 were harvested at OD₆₀₀ of 1.0 and resuspended in 100 μ l 1X LDS sample buffer (Novex),
745 containing 4% 2-mercaptoethanol (Sigma). Whole cells were treated with proteinase K as
746 previously described⁶². LPS samples were separated by 4-12% NUPAGE Bis-Tris gel and
747 visualized by silver staining (for *Ec* samples)⁶² or using ProQ Emerald 300 from Molecular
748 Probes (for *Cm*). For *E. coli* work only, all strains also contained plasmid pMF19 for
749 expression of WbbL, a rhamnosyltransferase required for O-antigen synthesis, as the *wbbL*
750 gene in K12 strains contain an IS5 insertion mutation.

751 **Statistics and Reproducibility.** For reproducibility all O-antigen ligase assay gels were run
752 in triplicates (**Fig. 2c, 4c, Extended Data Fig. 1c, 7a, and 7e**), all SDS page gels and
753 westerns were run in duplicates (**Extended data Fig. 1e, 7c and 7d**). The initial screen single
754 point ELISA to identify potential binders was carried out once (**Extended data Fig. 1g**), and
755 the multi-point sAB ELISA on the initial hits was run in triplicates (**Extended data Fig. 1h**).

756 **Bioinformatics sequence analysis and homology modelling *Ec*WaaL.** WaaL homologues
757 were identified using Hhblits⁶³, from the UniClust UniRef30 sequence database⁶⁴. The
758 resulting sequence alignment was illustrated using Weblogo3⁶⁵. Co-evolution analysis for
759 WaaL was performed using MapPred⁶⁶ and visualised with PyMOL. The Hhblits sequence
760 alignment, in combination with the model of *Ec*WaaL from the AlphaFold database²⁰, was
761 used to create and refine a pairwise sequence alignment between *Cm*WaaL and *Ec*WaaL. The
762 sequence alignment was visualised using ESPrpt⁶⁷. Modeller 9.24⁶⁸ was used to generate the

763 *Ec*WaaL homology model, with the co-evolutionary data used to evaluate the pairwise
764 residue distances in the resulting structure.

765 **Molecular dynamics simulations setup.** All simulations were run using GROMACS 2020⁶⁹.
766 The Martini 2.2 force field⁶⁹ was used to run a Coarse-Grained (CG) MD simulation to
767 permit the assembly and equilibration of a palmitoyl-oleoyl-phosphatidylglycerol (POPG)
768 and palmitoyl-oleoyl-phosphatidylethanolamine (POPE) (1:4 mole ratio) bilayer around
769 *Cm*WaaL⁷⁰ in the apo, Und-PP bound, Und-PP and lipid A core OS bound, or WaB10 Fab-
770 bound states. The initial glycerophospholipid bilayer was created using the *insane* python
771 script^{71,72} after which the *Cm*WaaL binding partners were added manually. An elastic
772 network of 1000 kJ mol⁻¹ nm⁻² was applied between all backbone beads between 0.5 and 1
773 nm. Electrostatics were described using the reaction field method, with a cut-off of 1.1 nm
774 using the potential shift modifier and the Van der Waals interactions were shifted between
775 0.9-1.1 nm. The systems were first energy minimised by steepest descent algorithm to 1000
776 kJ mol⁻¹ nm⁻² and then simulated for a total of 200 ns. Temperature and pressure were kept
777 constant throughout the simulation at 310 K and 1 bar respectively, with protein, lipids and
778 water/ions coupled individually to a temperature bath by the V-rescale method⁷³ and a semi-
779 isotropic Parrinello-Rahman barostat⁷⁴. The final snapshots from the CG simulations were
780 then converted back to an atomistic description using CG2AT2 using the protein-aligned
781 method⁷⁵.

782 **Atomistic molecular dynamics simulations.** All ionisable groups were simulated with
783 default protonation states, unless otherwise mentioned. The CHARMM36m forcefield⁷⁶ was
784 employed, with the use of a 2 fs time step during the simulations. Electrostatics were
785 described using PME, with a cut-off of 1.2 nm and the van der Waals interactions were
786 shifted between 1-1.2 nm. The TIP3P water model was used and water bond angles and

787 distances were constrained by SETTLE⁷⁷. All other bonds were constrained using the LINCS
788 algorithm⁷⁸. The systems were then equilibrated for an additional 1 ns using a 2 fs timestep,
789 with positional restraints of 1000 kJ mol⁻¹ nm⁻² on the protein heavy atoms, in an NPT
790 ensemble, with temperature V-rescale coupling at 310 K with protein, lipids and water/ions
791 coupled individually⁷³ and semi-isotropic Parrinello-Rahman barostat at 1 bar⁷⁴. Where
792 present during the equilibration, the non-hydrogen atoms of the first isoprenyl unit and
793 pyrophosphate were additionally restrained with positional restraints of 1000 kJ mol⁻¹ nm⁻²
794 applied to the coordinates taken from the cryo-EM structure. The parameters for Und-PP are
795 part of the CHARMM36m force field^{76,79}. The simulations for the four states were performed
796 without position restraints for a total of 500 ns and run in triplicate.

797 **Molecular dynamics simulation analysis.** RMSD and RMSF calculations were performed
798 on the backbone of *CmWaaL* using the `gmx rms` and `gmx rmsf` tools, respectively. The
799 dynamics of Und-PP over a total of 1.5 μ s were calculated on a per atom basis from the three
800 replicates via the `gmx rmsf` tool⁶⁹. The TM helix 9 movement was calculated via the distance
801 between the geometric centers of residues 184-295 and 229-245 using the PLUMED v2.5
802 software package⁸⁰. Membrane deformation was calculated by mapping the xy coordinates
803 for each phosphate over a total of 1.5 μ s of simulation onto a 1 Å resolution grid. The grid
804 represented by beads is coloured according to the deviation from the average membrane
805 phosphate z coordinate for each leaflet.

806

807

808

809

810

811

812
813
814
815
816
817
818
819
820
821
822
823
824
825
826
827

828 **Methods and Supplementary Material References**

829 31 Punta, M. *et al.* Structural genomics target selection for the New York consortium on
830 membrane protein structure. *Journal of structural and functional genomics* **10**, 255
831 (2009).

832 32 Mancía, F. & Love, J. High-throughput expression and purification of membrane
833 proteins. *Journal of structural biology* **172**, 85-93 (2010).

834 33 Mancía, F. & Love, J. High throughput platforms for structural genomics of integral
835 membrane proteins. *Current opinion in structural biology* **21**, 517-522 (2011).

- 836 34 Bayburt, T. H., Grinkova, Y. V. & Sligar, S. G. Self-assembly of discoidal
837 phospholipid bilayer nanoparticles with membrane scaffold proteins. *Nano letters* **2**,
838 853-856 (2002).
- 839 35 Denisov, I. G., Grinkova, Y. V., Lazarides, A. A. & Sligar, S. G. Directed self-
840 assembly of monodisperse phospholipid bilayer Nanodiscs with controlled size.
841 *Journal of the American Chemical Society* **126**, 3477-3487 (2004).
- 842 36 Kapust, R. B., Tözsér, J., Copeland, T. D. & Waugh, D. S. The P1' specificity of
843 tobacco etch virus protease. *Biochemical and biophysical research communications*
844 **294**, 949-955 (2002).
- 845 37 Rizk, S. S. *et al.* Allosteric control of ligand-binding affinity using engineered
846 conformation-specific effector proteins. *Nature structural & molecular biology* **18**,
847 437 (2011).
- 848 38 Miller, K. R. *et al.* T cell receptor-like recognition of tumor in vivo by synthetic
849 antibody fragment. *PloS one* **7**, e43746 (2012).
- 850 39 Dominik, P. K. *et al.* Conformational chaperones for structural studies of membrane
851 proteins using antibody phage display with nanodiscs. *Structure* **24**, 300-309 (2016).
- 852 40 Kim, J. *et al.* Structure and drug resistance of the Plasmodium falciparum transporter
853 PfCRT. *Nature* **576**, 315-320 (2019).
- 854 41 Suloway, C. *et al.* Automated molecular microscopy: the new Legimon system.
855 *Journal of structural biology* **151**, 41-60 (2005).
- 856 42 Slabinski, L. *et al.* XtalPred: a web server for prediction of protein crystallizability.
857 *Bioinformatics* **23**, 3403-3405 (2007).
- 858 43 Emsley, P. & Cowtan, K. Coot: model-building tools for molecular graphics. *Acta*
859 *crystallographica section D: biological crystallography* **60**, 2126-2132 (2004).

860 44 Emsley, P., Lohkamp, B., Scott, W. G. & Cowtan, K. Features and development of
861 Coot. *Acta Crystallographica Section D: Biological Crystallography* **66**, 486-501
862 (2010).

863 45 Casañal, A., Lohkamp, B. & Emsley, P. Current developments in Coot for
864 macromolecular model building of Electron Cryo- microscopy and Crystallographic
865 Data. *Protein Science* **29**, 1055-1064 (2020).

866 46 Afonine, P. V. *et al.* Towards automated crystallographic structure refinement with
867 phenix. refine. *Acta Crystallographica Section D: Biological Crystallography* **68**,
868 352-367 (2012).

869 47 Afonine, P. V. *et al.* Real-space refinement in PHENIX for cryo-EM and
870 crystallography. *Acta Crystallographica Section D: Structural Biology* **74**, 531-544
871 (2018).

872 48 Pettersen, E. F. *et al.* UCSF Chimera—a visualization system for exploratory research
873 and analysis. *Journal of computational chemistry* **25**, 1605-1612 (2004).

874 49 Goddard, T. D. *et al.* UCSF ChimeraX: Meeting modern challenges in visualization
875 and analysis. *Protein Science* **27**, 14-25 (2018).

876 50 Danilov, L., Druzhinina, T., Kalinchuk, N., Maltsev, S. & Shibaev, V. Polyprenyl
877 phosphates: synthesis and structure-activity relationship for a biosynthetic system of
878 *Salmonella anatum* O-specific polysaccharide. *Chemistry and physics of lipids* **51**,
879 191-203 (1989).

880 51 Jiang, W., Bikard, D., Cox, D., Zhang, F. & Marraffini, L. A. RNA-guided editing of
881 bacterial genomes using CRISPR-Cas systems. *Nature Biotechnology* **31**, 233-239,
882 doi:10.1038/nbt.2508 (2013).

883 52 Jiang, Y. *et al.* Multigene Editing in the *Escherichia coli* Genome via the CRISPR-
884 Cas9 System. *Applied and Environmental Microbiology* **81**, 2506-2514, (2015).

- 885 53 Selle, K. & Barrangou, R. Harnessing CRISPR–Cas systems for bacterial genome
886 editing. *Trends in Microbiology* **23**, 225-232, (2015).
- 887 54 Jiang, X. *et al.* Vector promoters used in *Klebsiella pneumoniae*. *Biotechnology and*
888 *Applied Biochemistry* **63**, 734-739, (2016).
- 889 55 Zhao, D. *et al.* Development of a fast and easy method for *Escherichia coli* genome
890 editing with CRISPR/Cas9. *Microbial Cell Factories* **15**, 205, (2016).
- 891 56 Wang, Y. *et al.* CRISPR-Cas9 and CRISPR-Assisted Cytidine Deaminase Enable
892 Precise and Efficient Genome Editing in *Klebsiella pneumoniae*. *Applied and*
893 *Environmental Microbiology* **84**, e01834-01818, (2018).
- 894 57 McConville, T. H. *et al.* CrrB Positively Regulates High-Level Polymyxin Resistance
895 and Virulence in *Klebsiella pneumoniae*. *Cell Reports* **33**, 108313, (2020).
- 896 58 Mijndonckx, K. *et al.* Characterization of the Survival Ability of *Cupriavidus*
897 *metallidurans* and *Ralstonia pickettii* from Space-Related Environments. *Microbial*
898 *Ecology* **65**, 347-360, (2013).
- 899 59 Schmidt, C., Schwarzenberger, C., Große, C. & Nies, D. H. FurC Regulates
900 Expression of for the Central Zinc Importer ZupT of *Cupriavidus metallidurans*.
901 *Journal of Bacteriology* **196**, 3461-3471, (2014).
- 902 60 Sambrook, J. & Rusell, D. *Molecular Cloning: A Laboratory Manual* 3rd Ed Cold
903 Spring Harbor Lab. Press, Plainview, New York (2001).
- 904 61 Baba, T. *et al.* Construction of *Escherichia coli* K- 12 in- frame, single- gene
905 knockout mutants: the Keio collection. *Molecular systems biology* **2**, 2006.0008
906 (2006).
- 907 62 Hitchcock, P. J. & Brown, T. M. Morphological heterogeneity among *Salmonella*
908 lipopolysaccharide chemotypes in silver-stained polyacrylamide gels. *Journal of*
909 *bacteriology* **154**, 269-277 (1983).

910 63 Remmert, M., Biegert, A., Hauser, A. & Söding, J. HHblits: lightning-fast iterative
911 protein sequence searching by HMM-HMM alignment. *Nature methods* **9**, 173-175
912 (2012).

913 64 Mirdita, M. *et al.* Uniclust databases of clustered and deeply annotated protein
914 sequences and alignments. *Nucleic acids research* **45**, D170-D176 (2017).

915 65 Crooks, G. E., Hon, G., Chandonia, J.-M. & Brenner, S. E. WebLogo: a sequence
916 logo generator. *Genome research* **14**, 1188-1190 (2004).

917 66 Wu, Q. *et al.* Protein contact prediction using metagenome sequence data and residual
918 neural networks. *Bioinformatics* **36**, 41-48 (2020).

919 67 Robert, X. & Gouet, P. Deciphering key features in protein structures with the new
920 ENDscript server. *Nucleic acids research* **42**, W320-W324 (2014).

921 68 Šali, A. & Blundell, T. L. Comparative protein modelling by satisfaction of spatial
922 restraints. *Journal of molecular biology* **234**, 779-815 (1993).

923 69 Abraham, M. J. *et al.* GROMACS: High performance molecular simulations through
924 multi-level parallelism from laptops to supercomputers. *SoftwareX* **1**, 19-25 (2015).

925 70 Vogeley, L. *et al.* Structural basis of lipoprotein signal peptidase II action and
926 inhibition by the antibiotic globomycin. *Science* **351**, 876-880 (2016).

927 71 Wassenaar, T. A., Ingólfsson, H. I., Böckmann, R. A., Tieleman, D. P. & Marrink, S.
928 J. Computational lipidomics with insane: a versatile tool for generating custom
929 membranes for molecular simulations. *Journal of chemical theory and computation*
930 **11**, 2144-2155 (2015).

931 72 <https://github.com/Tsjerk/Insane>.

932 73 Bussi, G., Donadio, D. & Parrinello, M. Canonical sampling through velocity
933 rescaling. *The Journal of chemical physics* **126**, 014101 (2007).

934 74 Parrinello, M. & Rahman, A. Polymorphic transitions in single crystals: A new
935 molecular dynamics method. *Journal of Applied physics* **52**, 7182-7190 (1981).

936 75 Stansfeld, P. J. & Sansom, M. S. From coarse grained to atomistic: a serial multiscale
937 approach to membrane protein simulations. *Journal of chemical theory and*
938 *computation* **7**, 1157-1166 (2011).

939 76 Huang, J. *et al.* CHARMM36m: an improved force field for folded and intrinsically
940 disordered proteins. *Nature methods* **14**, 71-73 (2017).

941 77 Miyamoto, S. & Kollman, P. A. Settle: An analytical version of the SHAKE and
942 RATTLE algorithm for rigid water models. *Journal of Computational Chemistry* **13**,
943 952-962, (1992).

944 78 Hess, B., Bekker, H., Berendsen, H. J. C. & Fraaije, J. G. E. M. LINCS: A linear
945 constraint solver for molecular simulations. *Journal of Computational Chemistry* **18**,
946 1463-1472, (1997).

947 79 Jo, S., Kim, T., Iyer, V. G. & Im, W. CHARMM-GUI: A web-based graphical user
948 interface for CHARMM. *Journal of Computational Chemistry* **29**, 1859-1865, (2008).

949 80 Bonomi, M. *et al.* Promoting transparency and reproducibility in enhanced molecular
950 simulations. *Nature methods* **16**, 670-673 (2019).

951 81 Whitney, J. & Howell, P. Synthase-dependent exopolysaccharide secretion in Gram-
952 negative bacteria. *Trends in microbiology* **21**, 63-72 (2013).

953 82 Whitfield, C. Biosynthesis and assembly of capsular polysaccharides in *Escherichia*
954 *coli*. *Annu. Rev. Biochem.* **75**, 39-68 (2006).

955 83 Cuthbertson, L., Kos, V. & Whitfield, C. ABC transporters involved in export of cell
956 surface glycoconjugates. *Microbiology and Molecular Biology Reviews* **74**, 341-362
957 (2010).

958 84 Pérez-Burgos, M. *et al.* Characterization of the exopolysaccharide biosynthesis
959 pathway in *Myxococcus xanthus*. *Journal of bacteriology* **202** (2020).

960 85 Mi, W. *et al.* Structural basis of MsbA-mediated lipopolysaccharide transport. *Nature*
961 **549**, 233-237 (2017).

962 86 Fellouse, F. A. *et al.* High-throughput generation of synthetic antibodies from highly
963 functional minimalist phage-displayed libraries. *Journal of molecular biology* **373**,
964 924-940 (2007).

965 87 Rubinstein, J. L. & Brubaker, M. A. Alignment of cryo-EM movies of individual
966 particles by optimization of image translations. *Journal of structural biology* **192**,
967 188-195 (2015).

968

969 **Acknowledgements**

970 We gratefully acknowledge the assistance of members of the Mancia lab, and of the
971 Columbia University cryo-EM facility. We would like to thank Professor Gideon Davies,
972 University of York, for his precious input on the glycosyl transferase mechanism. This work
973 was funded by NIH grants GM132120 (to F.M.), AI150098, AI138576, and AI129940 (to
974 M.S.T.), GM117372 (to A.A.K.) and GM116799 (to Wayne A. Hendrickson), U54
975 DK104309 (ACU), T32 AI100852, and K08 AI146284 (THM). Research in P.J.S.'s lab was
976 funded by Wellcome (208361/Z/17/Z), the MRC (MR/S009213/1) and BBSRC
977 (BB/P01948X/1, BB/R002517/1 and BB/S003339/1). This project made use of time on
978 ARCHER and JADE granted via the UK High-End Computing Consortium for Biomolecular
979 Simulation, HECBioSim (<http://hecbiosim.ac.uk>), supported by EPSRC (grant no.
980 EP/R029407/1). P.J.S. acknowledges Athena and Sulis at HPC Midlands+, which were
981 funded by the EPSRC on grants EP/P020232/1 and EP/T022108/1, and the University of
982 Warwick Scientific Computing Research Technology Platform for computational access.
983 C.L.B.G. is funded by BBSRC studentship grant BB/M01116X/1 and D.I.R. is funded by a
984 Schaefer Research Scholars Program Awards to Columbia University and MRC grant
985 MR/N002679/1. Some of the work was performed at the Center for Membrane Protein
986 Production and Analysis (COMPPÅ) and at the National Resource for automated Molecular
987 Microscopy at the National Resource for Molecular Microscopy at the Simons Electron
988 Microscopy Center, both located at the New York Structural Biology Center.

989 **Author contributions**

990 K.U.A. with help from B.K., M.B.D. and A.P.Z., performed the genomic expansion
991 screen, protein expression and purification. S.K.E., K.N. and A.A.K. identified and purified
992 the Fabs. K.U.A. produced and analyzed the cryo-EM data, and built the model with help

993 from O.B.C.. Mutational analysis were performed by K.U.A., V.I.P. and S.I.G.. Gene editing
994 for *Cupriavidus metallidurans* were performed by T.H.M. and A.C.U.. Assessment of WaaL
995 function was carried out by C.M.H and M.S.T.. All molecular dynamics simulations were
996 performed by P.J.S. and O.N.V.. The ligands for TLC analysis were synthesized by K.S.T.
997 under the guidance of E.S., and K.U.A. performed the TLC analysis. K.U.A., F.M., P.J.S.,
998 O.N.V., C.M.H., and M.S.T. designed experiments and wrote the paper with R.N., C.L.B.G.,
999 and D.I.R.. Oversight for the entire project was provided by F.M.

1000 **Competing interests**

1001 The authors declare no competing interests.

1002 **Correspondence and requests for materials**

1003 Should be addressed to strent@uga.edu (M.S.T.), phillip.stansfeld@warwick.ac.uk (P.J.S.) or
1004 fm123@cumc.columbia.edu (F.M.).

1005 **Data availability**

1006 All raw movie frames have been deposited into EMPIAR, with accession code
1007 EMPIAR-10938. The density maps have been deposited into EMDB, with accession code
1008 EMD-26054 for the Und-PP bound *CmWaaL* and EMD-26057 for the apo *CmWaaL*. Both
1009 models have been deposited in the PDB, with accession code 7TPG for the Und-PP bound,
1010 and 7TPJ for the apo *CmWaaL* model. All raw gels are available in the supplementary
1011 information.

1012

1013

1014

1015 **Extended Data Figure Legends**

1016 **Extended Data Table 1 | Cryo-EM Data.** Cryo-EM data collection, refinement and
1017 validation statistics.

1018

1019 **Extended Data Figure 1 | Functional validation of *CmWaaL*, identification of WaaL-**
1020 **specific Fabs and preparation of nanodisc-reconstituted WaaL-Fab complex for**

1021 **structural analysis. a,** Schematic representation of O-antigen synthesis and transfer to the

1022 periplasmic leaflet of the inner membrane by the three different pathways, the arrows

1023 represent the direction of the Und-PP linked O-antigen takes in each pathway. Individual

1024 lipid-linked O-antigen repeat units are ligated to the lipid carrier Und-PP by

1025 glycosyltransferase enzymes. In the Wzy-dependent pathway, the O units are transported into

1026 the periplasm by the flippase Wzx. Wzy then catalyses the polymerization of O-antigen

1027 repeats, while Wzz controls the preferred modal length of the final O-antigen polymer⁹. The

1028 synthase dependent pathway is the least well characterized pathway⁸¹, the O-antigen is

1029 assembled at the cytoplasmic face of the inner membrane by a synthase that is also involved

1030 in its transportation across the membrane. In the ABC-dependent pathway, the polymerized

1031 Und-PP-O-antigen molecule is flipped to the periplasmic face of the inner membrane by an

1032 ABC transporter, Wzm-Wzt flippase⁸¹⁻⁸⁴. It is important to note that the chemical

1033 composition of the *C. metallidurans* O-antigen is unknown. **b,** Schematic of WaaL function.

1034 On the right, the lipid A core OS is synthesized in the cytoplasm and flipped to the periplasm

1035 via MsbA⁸⁵. On the left, the lipid A core OS and the O-antigen, irrespective of the pathway of

1036 origin, are ligated by WaaL. **c,** Functional analysis of *CmWaaL* ligase activity in whole cells.

1037 LPS gel showing that O-antigen ligase activity is abolished when *Cm waaL* is deleted, and

1038 activity is restored by plasmid complementation. **d,** Size exclusion chromatography elution

1039 profiles of purified *CmWaaL* in detergent (blue), *CmWaaL* incorporated into a nanodisc

1040 (red), and *CmWaaL* incorporated into a nanodisc with Fab (WaB10) bound (black). **e**, SDS-
1041 PAGE gel of *CmWaaL* purification. First lane is *CmWaaL* purified in DDM, second lane is
1042 *CmWaaL* reconstituted into nanodiscs (MSP1E3D1 and POPG), and third lane is *CmWaaL*
1043 reconstituted into nanodiscs (MSP1E3D1 and POPG) with Fab (WaB10) bound. **f**,
1044 Complementarity-determining region (CDR) sequences of unique synthetic antigen binders
1045 (sABs) from biopanning against *CmWaaL* in MSP1E3D1 nanodiscs. sABs were selected
1046 following multiple rounds of phage display starting from Fab Library E^{37,38}. Enriched YSGW
1047 residues are highlighted by coloured boxes (yellow, red, green, and blue, respectively).
1048 YSGW residues have been previously shown to play dominant roles in highly specific and
1049 high affinity antigen recognition⁸⁶. **g**, Single-point ELISA measuring the binding of phage-
1050 displayed sABs to *CmWaaL* in MSP1E3D1 nanodiscs (red), empty nanodiscs (light grey), or
1051 buffer (empty wells, dark grey). ELISA signal measured at 450 nm absorbance, see
1052 Supplementary Table 1. **h**, Multi-point sAB ELISA: EC₅₀ estimation for purified sAB
1053 binding to *CmWaaL* incorporated into MSP1E3D1 nanodiscs, showing high affinity binding
1054 of WaE8 (green, 6.6±0.045 nM), WaB10 (red, 1.87±0.07 nM), WaC9 (orange, 6.26±0.18
1055 nM), WaG11 (cyan, 3.31±0.06 nM), and WaC10 (magenta, 3.90±0.09 nM), and modest
1056 affinity binding of WaF10 (blue, 279.5±0.68 nM) and WaB12 (brown, 154±0.11 nM), see
1057 Supplementary Table 1. EC₅₀ values represent the mean of three independent experiments +/-
1058 standard error (n=3).

1059

1060 **Extended Data Figure 2 | Cryo-EM analysis of the *CmWaaL*-Fab complex.** **a**, Flow chart
1061 outlining cryo-EM data processing and refinement performed to obtain a structure of a
1062 nanodisc-reconstituted *CmWaaL* with the Fab WaB10, both for the apo and the Und-PP
1063 bound structures. **b**, On the left, representative micrograph (2.44 µm defocus). On right,
1064 representative two-dimensional class averages from CryoSPARC two-dimensional

1065 classification^{86,87}. **c**, Fourier shell correlation (FSC) curves for the Und-PP bound *CmWaaL*-
1066 Fab complex. **d**, Local resolution display of unsharpened reconstructions of Und-PP bound
1067 *CmWaaL* in complex with the WaB10 Fab, in orthogonal views. **e**, Euler angle distribution of
1068 all Und-PP bound particles used in the final map reconstruction. Final map shown in green.
1069 Each orientation is represented by a cylinder, with each cylinder's height and color (from
1070 blue to red) proportional to the number of particles for that specific direction.

1071

1072 **Extended Data Figure 3 | Fit of cryo-EM density with model.** Cryo-EM densities (mesh)
1073 are superimposed on TM and PH helices of the *CmWaaL* model. The model is rendered as
1074 sidechain, coloured in rainbow, as in **Fig. 1d**. Und-PP (gold) is shown as sticks.

1075

1076 **Extended Data Figure 4 | Interaction of *CmWaaL* and Fab in the complex, and**
1077 **Sequence Alignment WebLogo.** **a**, *CmWaaL*-WaB10 complex structure shown in ribbon
1078 with WaaL in grey and WaB10 in pink. Only the variable domain of WaB10 was modelled
1079 into the map. **b**, Interface between *CmWaaL* (grey) and WaB10 (pink). Residues shown in
1080 sticks (I137, D245, S261 for *CmWaaL*, and N31, Y93, F104 for Fab). **c**, A Weblogo for
1081 orthologues of *CmWaaL* annotated with TM and soluble helices. The numbering for
1082 *CmWaaL* is shown.

1083

1084 **Extended Data Figure 5 | Structural features and analysis of *CmWaaL*.** **a**, *CmWaaL*
1085 rendered in surface representation coloured by electrostatic potential on a range of ± 5
1086 kBT/e. **b**, *CmWaaL* surface coloured by Wimley-White hydrophobicity, on a cyan (very
1087 hydrophilic) to gold (very hydrophobic) scale. **c**, *CmWaaL* surface coloured by residue
1088 conservation on a green (no conservation) to purple (absolute conservation) scale. **d**, TLC
1089 analysis of detergent purified *CmWaaL*. *CmWaaL* was purified in detergent and run on the

1090 TLC plate after organic-phase extraction of lipids. POPG, Und-P, Und-PP and an unrelated
1091 control protein expressed in *E. coli* were run in separate lanes as standards. MCR-1 was
1092 chosen as it utilizes a lipid donor (phosphatidylethanolamine) to modify the lipid A domain
1093 of LPS, but does not utilize Und-PP. **e**, Und-PP binding site. Residues coordinating the first
1094 two isoprenyls in the Und-PP tail, shown as sticks (blue). Und-PP shown as sticks coloured
1095 golden. **f**, (Top) MD simulations showing the Und-PP binding to *CmWaaL* from two views,
1096 and the flexibility of the Und-PP tail beyond the first two isoprenyl groups. The Und-PP
1097 shows increasing mobility away from the pyrophosphate. Here, the Root Mean Squared
1098 Fluctuation (RMSF) of Und-PP is shown for 3 repeats of 500 ns simulation. The non-
1099 hydrogen atoms of Und-PP are coloured by RMSF from blue to red. (Bottom) The RMSF of
1100 all atoms of the Und-PP are shown. The portion of the Und-PP resolved in the cryo-EM
1101 density map is highlighted in red.

1102

1103 **Extended Data Figure 6 | *EcWaaL* homology model. a**, Co-evolutionary analysis for
1104 *CmWaaL* calculated using MapPred and mapped onto the cryo-EM structure of *CmWaaL*,
1105 using a threshold of 0.2⁶⁶. Predicted contacts between C α atoms of given residues are shown
1106 as dashes for distances less than 10 Å (green), between 10 and 12 Å (cyan), between 12 and
1107 20 Å (yellow), and above 20 Å (red). The *CmWaaL* structure is shown as a grey ribbon
1108 representation. **b**, Comparison of the *CmWaaL* structure with the homology model of
1109 *EcWaaL*, both coloured in rainbow from N- to C-termini. Und-PP is shown bound to both
1110 structures and coloured in gold, as well as the key arginine residues that surround Und-PP,
1111 show as sticks. **c**, Sequence alignment and secondary structure of *CmWaaL* and *EcWaaL*.
1112 Conserved residues are highlighted in black.

1113

1114 **Extended Data Figure 7 | Analysis of *CmWaaL* and *EcWaaL* ligase activity.** **a**,
1115 Functional analysis of *EcWaaL* ligase activity in whole cells by LPS gel analysis. *Ec* LPS
1116 profile. W3110 $\Delta waaL$ containing either empty vector pWSK29 (\emptyset), pWSK29::*EcWaaL*
1117 (WT) or pWSK19::*EcWaaL*-variants¹⁰¹ was evaluated for O-antigen extension. W3110
1118 *EcWaaL* point mutations that cause loss of ligase activity. **b**, Table showing key residues in
1119 *CmWaaL* and their corresponding residues in *EcWaaL*. **c**, SDS-PAGE gel of all *EcWaaL*
1120 mutants that were purified to verify expression. **d**, Western blot analysis, using a mouse
1121 monoclonal anti-Flag antibody, of Flag purified WT *CmWaaL* and mutants, grown in *C.*
1122 *metallidurans*. **e**, Functional analysis of *CmWaaL* ligase activity in whole cells by LPS gel
1123 analysis *C. metallidurans* $\Delta waaL$ containing either empty vector pBBR1(\emptyset),
1124 pBBR1:*CmWaaL* (WT) or pBBR1:*CmWaaL*-variants was evaluated for O-antigen extension.
1125 **f**, Top view of *EcWaaL* showing the residues mutated in the two right panels in panel **a**. **g**,
1126 Top view of the *EcWaaL* model, highlighting T170 (left panel) and when mutated to Trp
1127 (right panel). **h**, Representative views of lipid A bound to *EcWaaL* within the interface of
1128 cavity 2 (left panel) and an alternative binding site within the Und-PP pocket of cavity 1
1129 (right panel). Lipid A-core shown as sticks, Und-PP (gold) and H338 shown as spheres.

1130

1131 **Extended Data Figure 8 | Comparison of the Und-PP bound and the apo WaaL *Cm***
1132 **structures.** **a**, Top Views of the Und-PP bound (grey) and the apo (pink) *CmWaaL*
1133 structures, showing the density (mesh) of the Und-PP (yellow) in the ligand bound structure
1134 in comparison to the apo, structure. **b**, Cryo-EM density maps for the Und-PP bound (grey)
1135 and the apo (pink) *CmWaaL*. Density maps were prepared in chimeraX⁴⁹, by deleting any
1136 density within a 4 Å radius of the Fab in the final model. **c**, Side views of the Und-PP bound
1137 (grey) and the apo (pink) *CmWaaL* shown as ribbon. The Und-PP (yellow) is shown as sticks
1138 in the bound structure. **d**, Top views of the Und-PP bound (grey) and the apo (pink) *CmWaaL*

1139 showing the key residues that we hypothesize play a role in either binding/shuttling or
1140 ligation of the substrates. The density for the selected residues is shown as grey mesh. On the
1141 right an overlay of bound and apo states are shown with highlighted residues shown in stick
1142 representation.

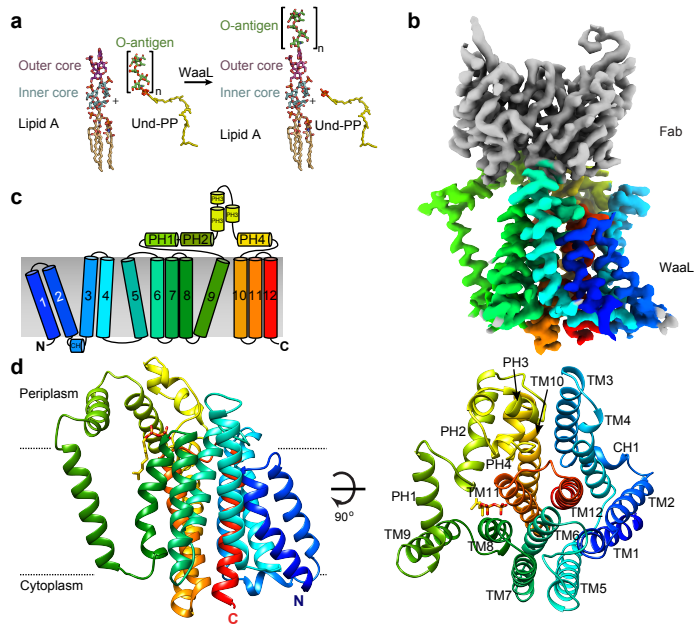
1143

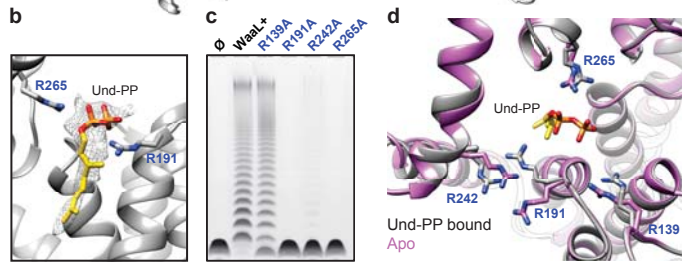
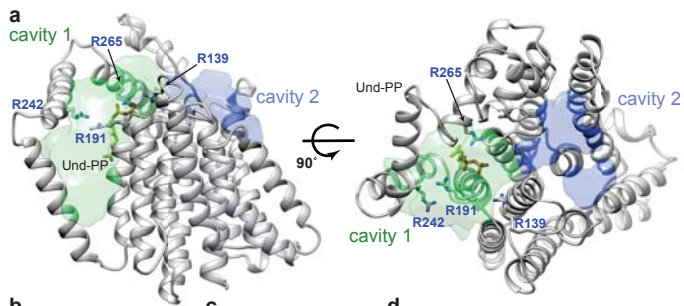
1144 **Extended Data Figure 9 | *CmWaaL* Molecular Dynamics Simulations. a,** The RMSF of
1145 the backbone of *CmWaaL*. The RMSF measurements were averaged across 3 repeats of 500
1146 ns simulation. The grey shading refers to the standard deviation across the repeats. Two
1147 highly mobile domains are highlighted in yellow (TM helix 9 and PH1) and purple (PH3).
1148 These domains have been highlighted on the ribbon structure for reference. The ribbon
1149 structures shown are coloured by their respective RMSF from blue to red. **b,** Representative
1150 frames for the closed (red) and open (blue) states are shown, derived from the simulations.
1151 The mobility of TM helix 9 is demonstrated by the histograms of the distance between the
1152 geometric centers of residues 229-244 and 184-195. The simulations of *CmWaaL* with Und-
1153 PP bound show a stabilisation of the closed state, while TM helix 9 separates from the core
1154 of *CmWaaL* in the apo state, opening an access channel to the active site. The initial distance
1155 from the cryo-EM structure is highlighted by a black line.

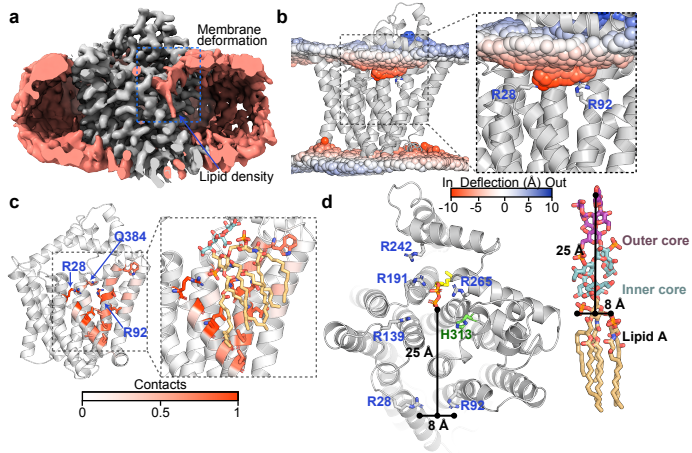
1156

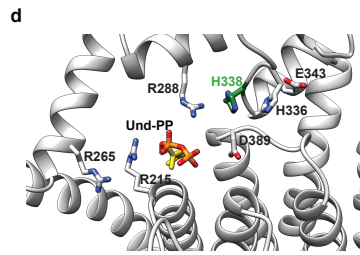
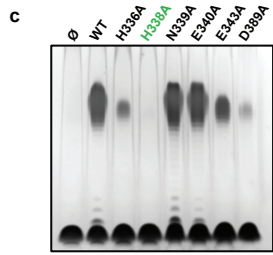
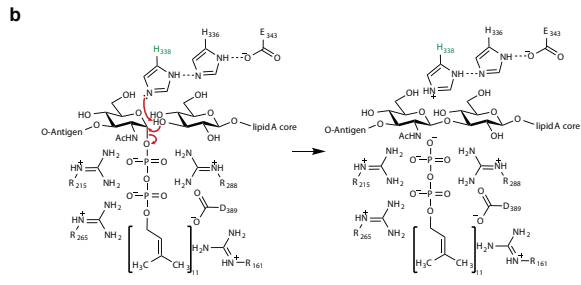
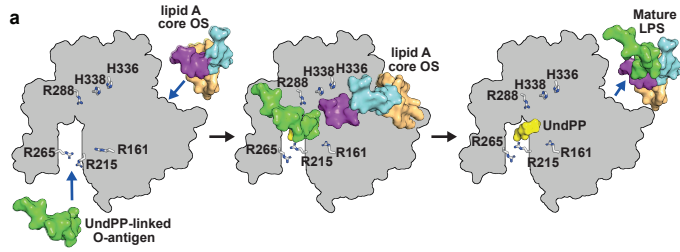
1157 **Extended Data Figure 10 | A putative common shuttling mechanism between *CmWaaL*,**
1158 **RodA, ArnT and PglB. a,** Structural comparison between *CmWaaL* and *TtRodA* (PDB ID
1159 6PL5), coloured on a blue to red rainbow from N- to C-terminus. The two additional helices
1160 (TMs 1 and 2) of *CmWaaL* are in grey. **b,** A comparison of the putative access pathway for
1161 polyprenyl-linked-phosphate containing ligands for *CmWaaL*, *TtRodA*, *CmArnT* (PDB ID
1162 5F15) and *CtPglB* (PDB ID 5OGL). The equivalent TM helix is shown in red and
1163 periplasmic helix in blue. Conserved residues, that may be involved in the shuttling and/or

- 1164 coordination of polyprenyl-phosphate containing ligands in *CmWaaL*, *TiRodA*, *CmArnT* and
1165 *CIPglB* are shown in sticks and highlighted in blue.

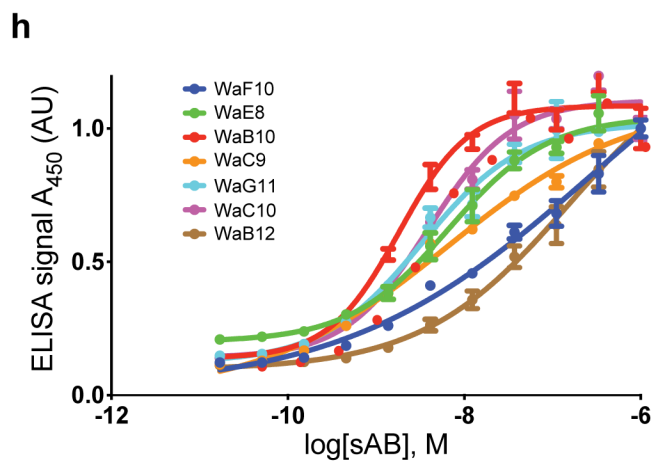
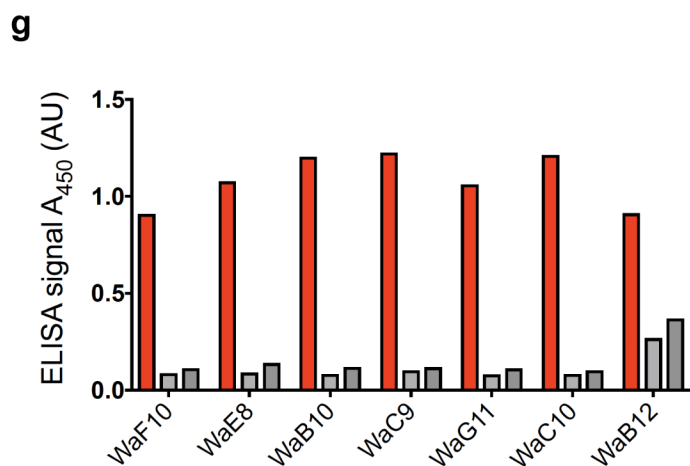
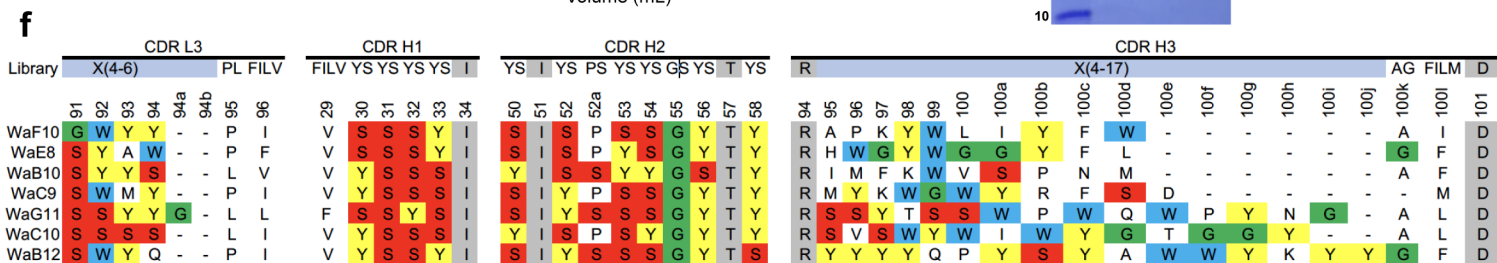
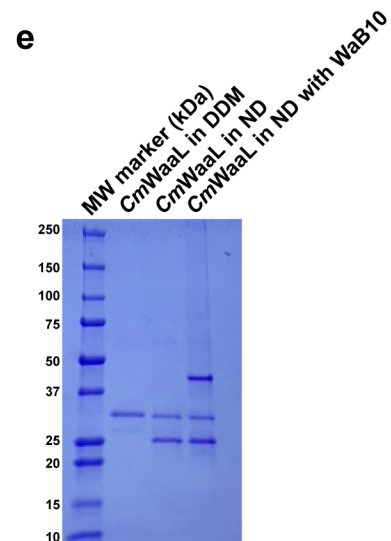
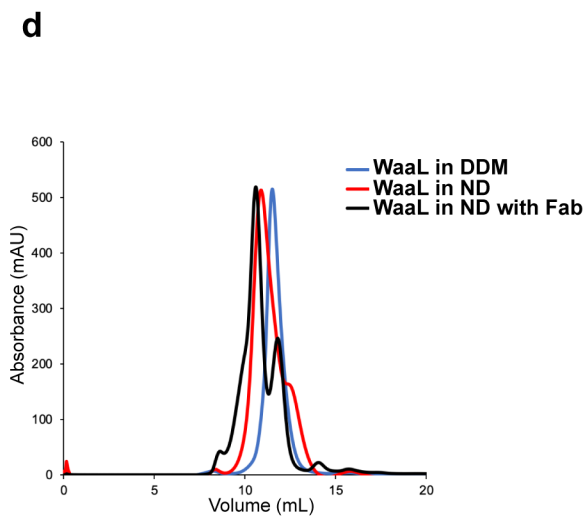
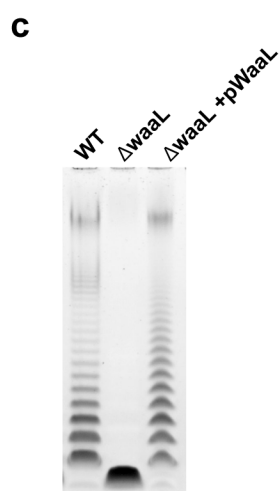
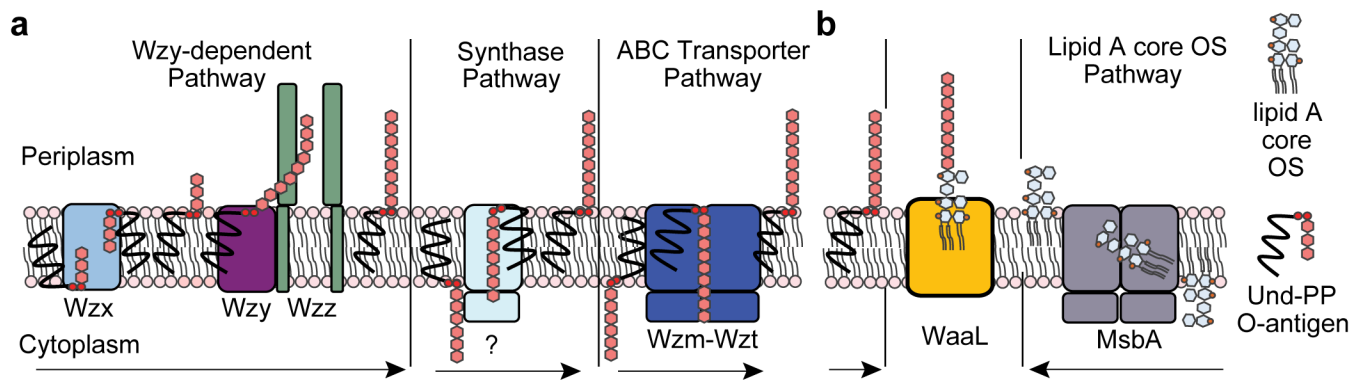


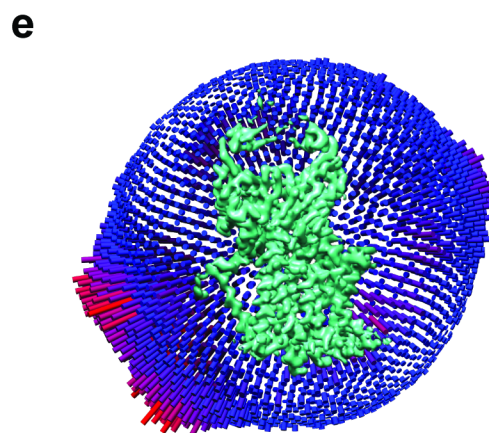
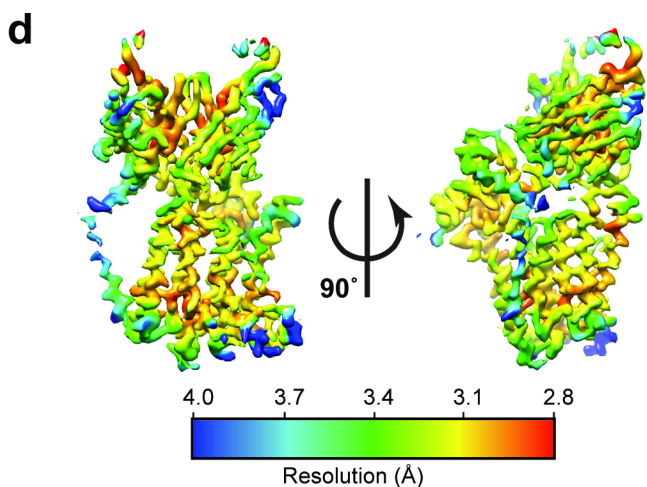
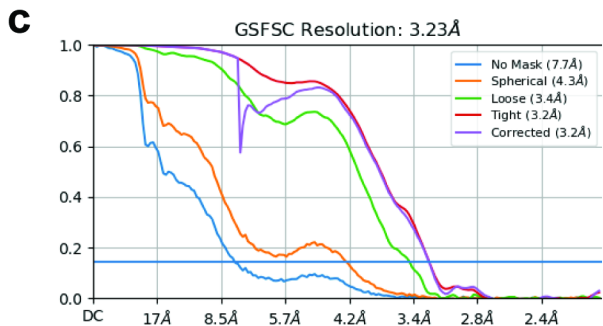
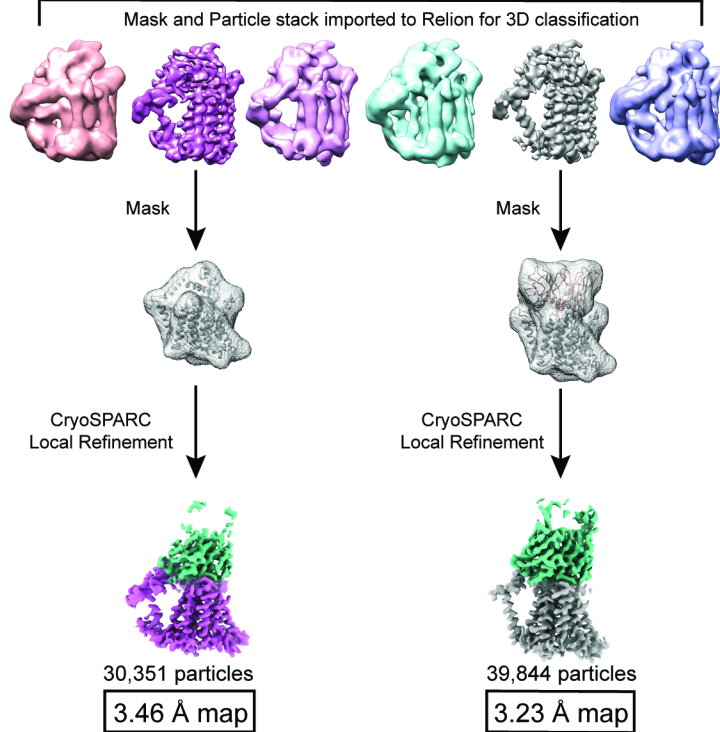
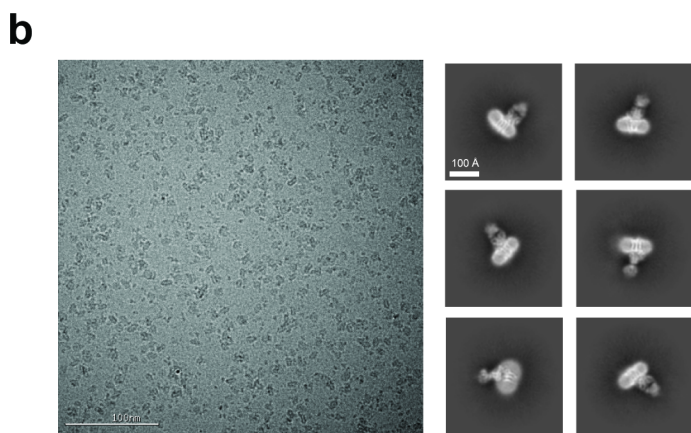
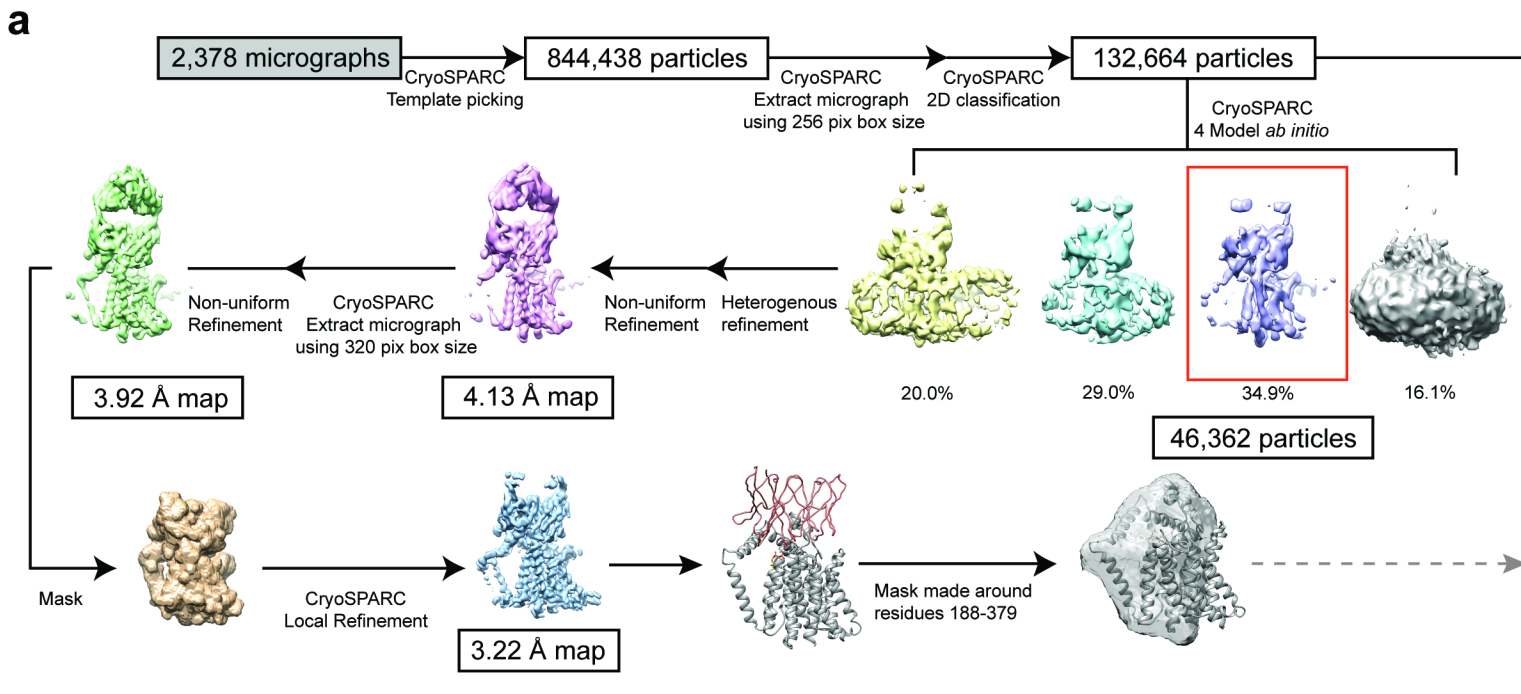


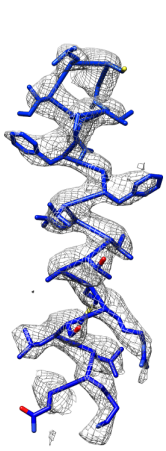




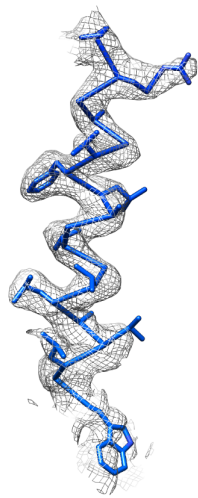
	WaaL-WaB10 (Und-PP bound) (EMD – 26054) (PDB – 7TPG)	WaaL-WaB10 (apo) (EMD – 26057) (PDB – 7TPJ)
Data collection and processing		
Magnification	130,000	13,000
Voltage (kV)	300	300
Electron exposure (e-/Å ²)	70	70
Exposure time (s)	2.5	2.5
Dose rate (e-/pixel/s)	16	16
Nominal defocus range (μm)	1-2	1-2
Defocus range (μm)	0.8-1.2	0.8-1.2
Pixel size (Å)	1.061	1.061
Symmetry imposed	C1	C1
Number of micrographs	2,378	2,378
Initial particle images (no.)	844,438	844,438
Final particle images (no.)	39,844	30,514
Map resolution (Å)	3.23	3.46
FSC threshold	0.143	0.143
Sphericity of 3DFSC	0.944	0.944
Refinement		
Map sharpening <i>B</i> factor (Å ²)	-24.07	-12.22
Residue range	5-407 (<i>Cm</i> WaaL) 2-105 and 5-123 (Fab)	
Model composition		
Non-hydrogen atoms	4778	4759
Protein residues	626	626
Ligands	1	0
<i>B</i> factors (Å²)		
Protein	43.04	35.95
Ligand	61.05	---
R.m.s. deviations		
Bond lengths (Å)	0.002	0.004
Bond angles (°)	0.621	0.700
Validation		
MolProbity score	1.63	1.83
Clashscore	7.19	9.09
Poor rotamers (%)	0.20	0.00
EM-Ringer Score	2.45	1.60
Ramachandran plot		
Favored (%)	96.45	95.00
Allowed (%)	3.55	5.00
Disallowed (%)	0.00	0.00



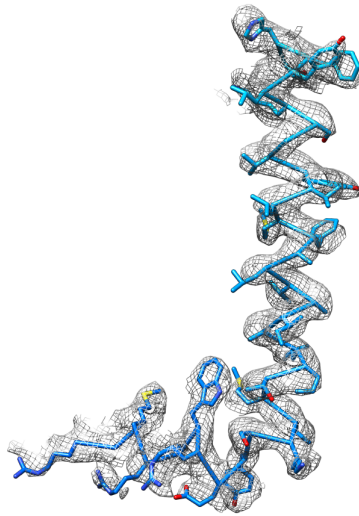




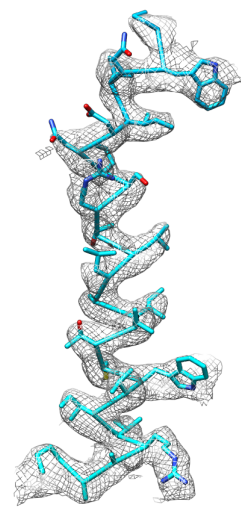
TM1 (5-26)



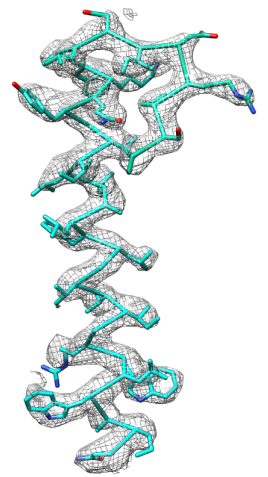
TM2 (27-45)



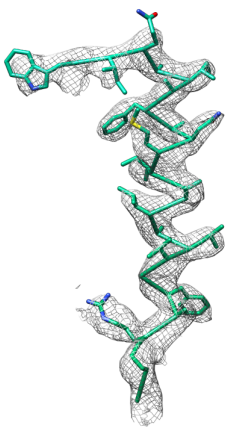
CH & TM3 (46-82)



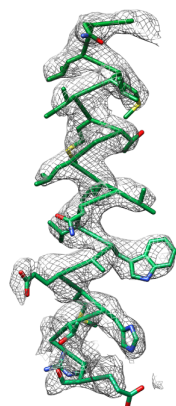
TM4 (83-108)



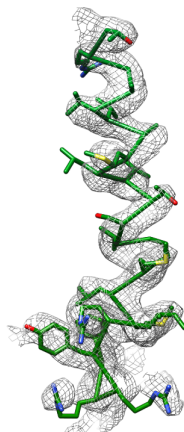
TM5 (109-142)



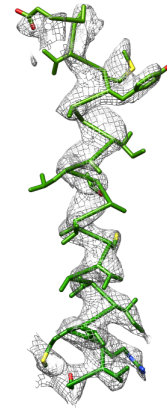
TM6 (143-165)



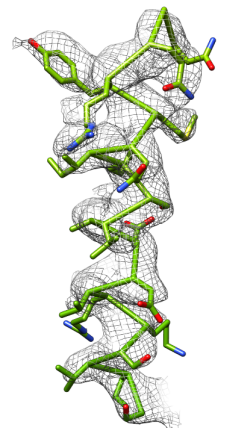
TM7 (166-189)



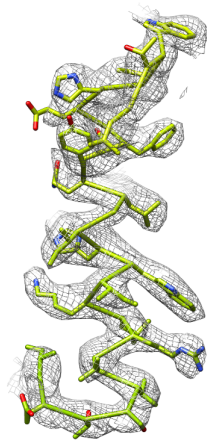
TM8 (190-212)



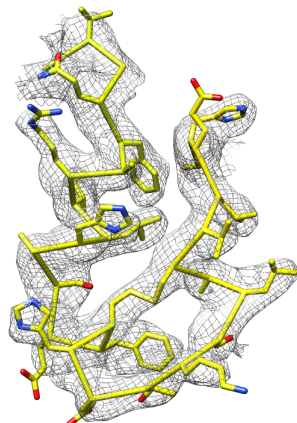
TM9 (213-236)



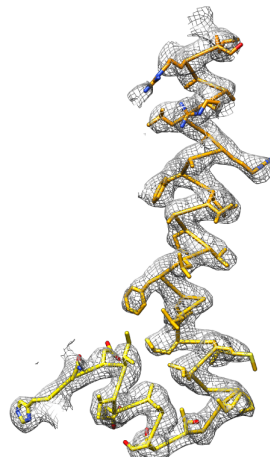
PH1 (237-257)



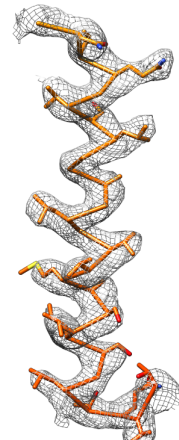
PH2 (258-284)



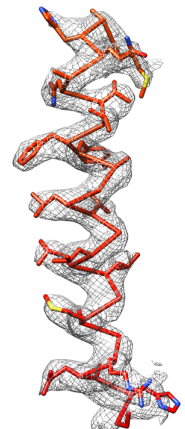
PH3 (285-312)



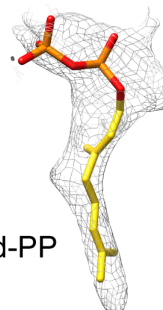
PH4 & TM10 (313-352)



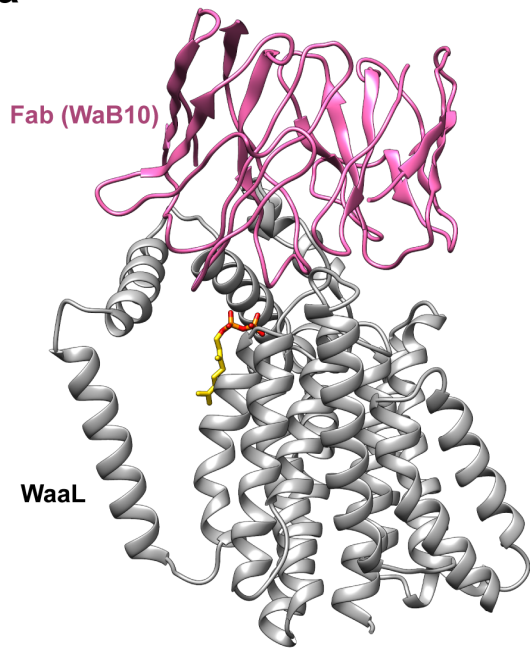
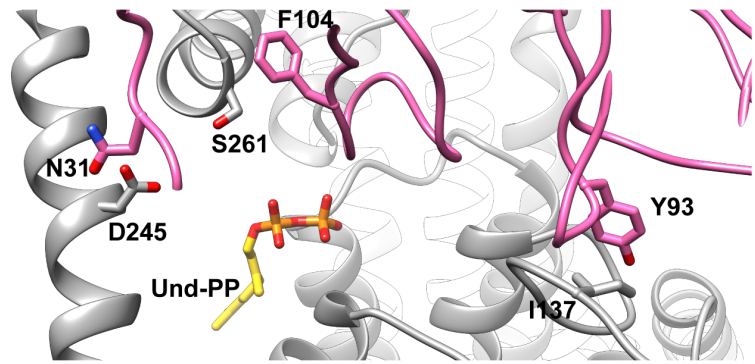
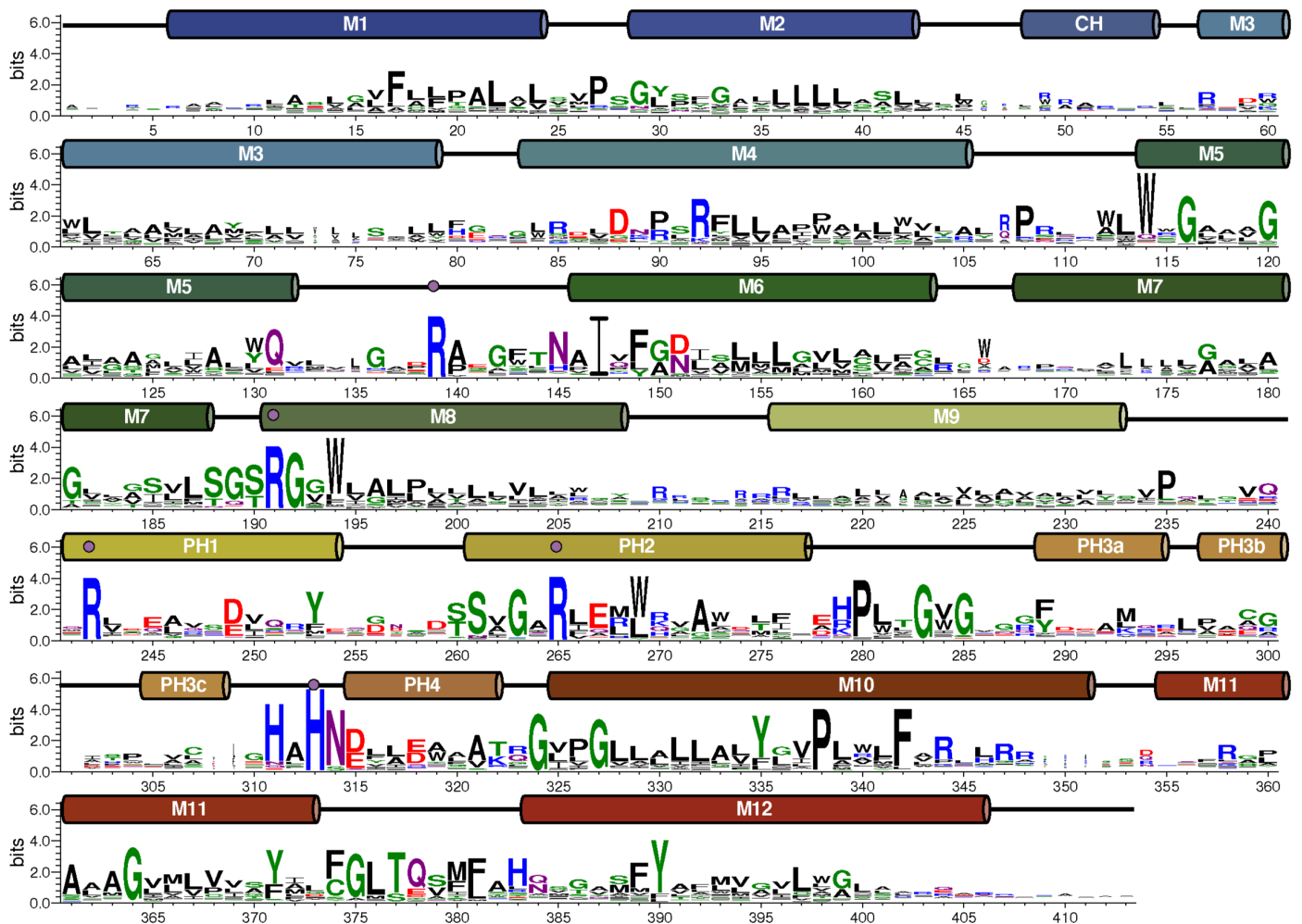
TM11 (353-380)

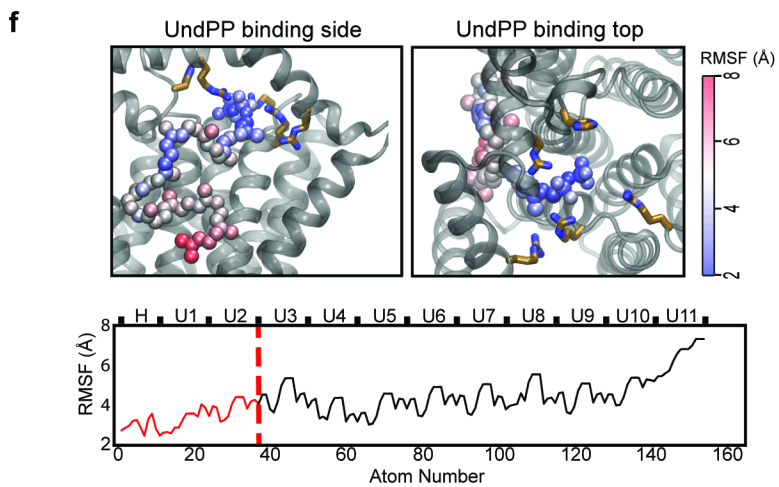
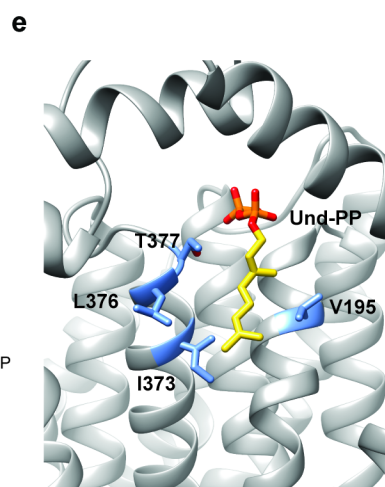
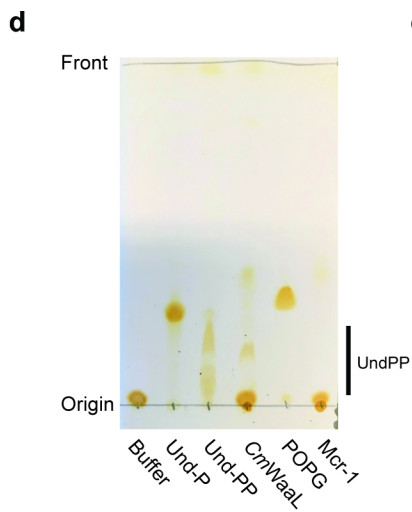
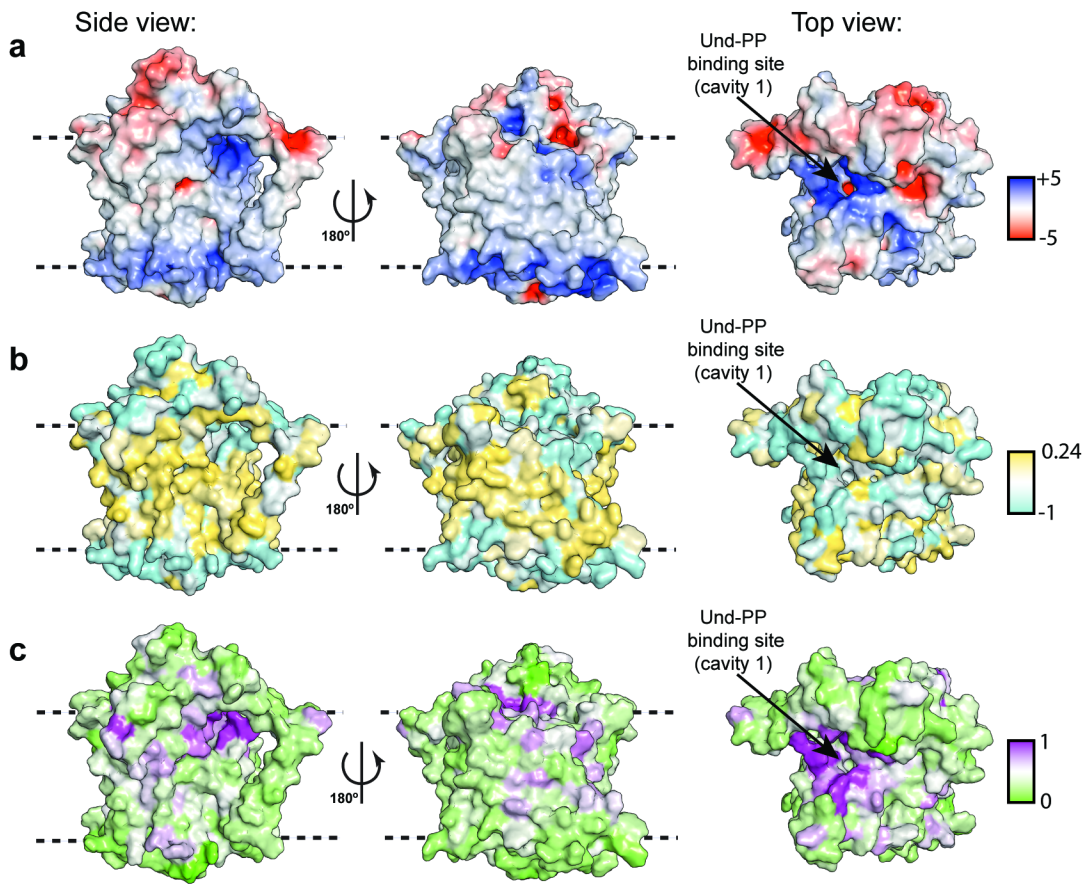


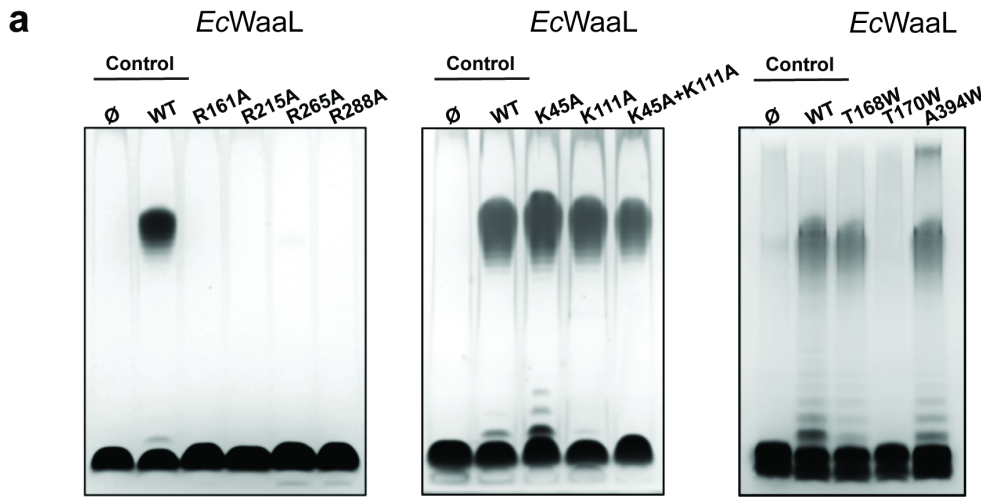
TM12 (381-407)



Und-PP

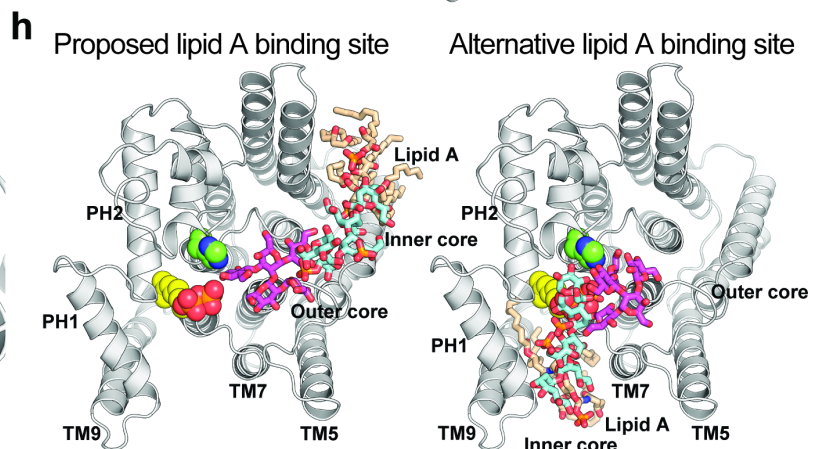
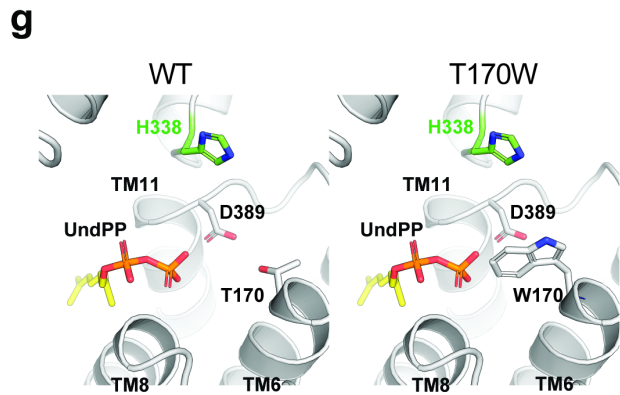
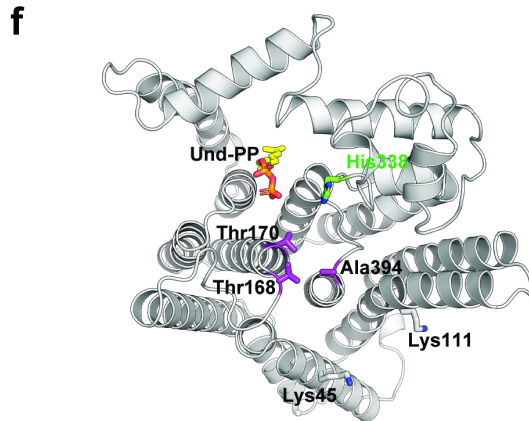
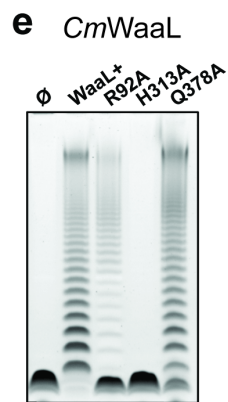
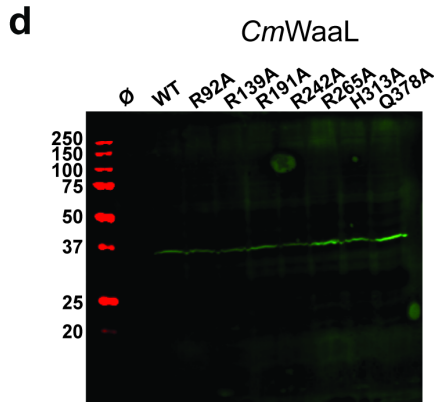
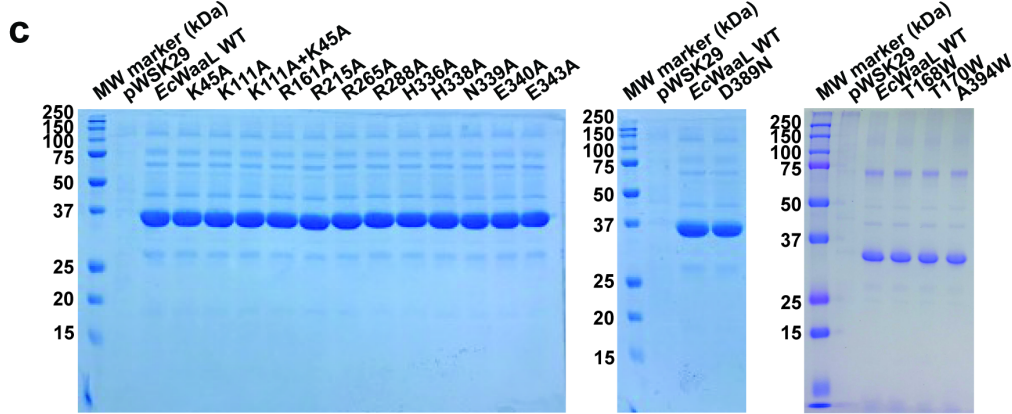
a**b****c**

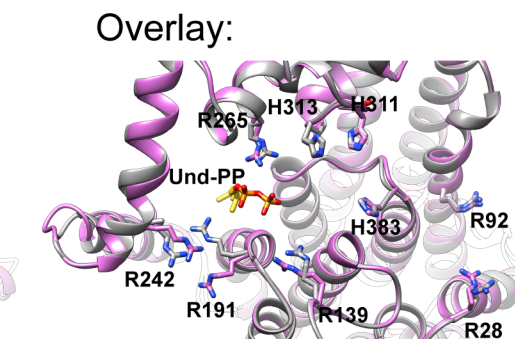
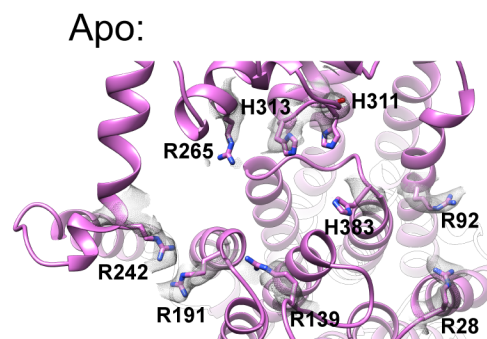
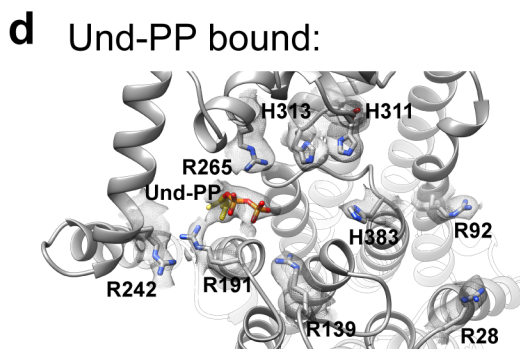
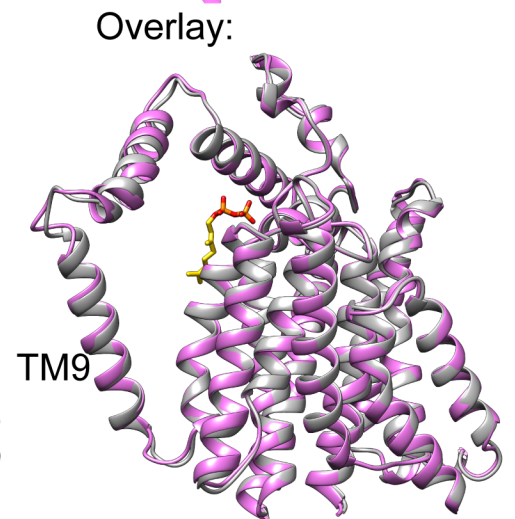
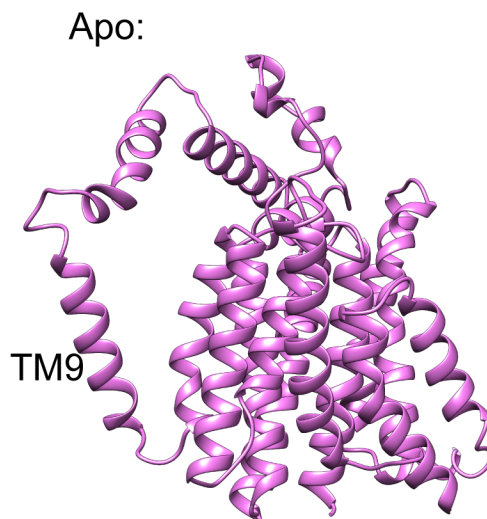
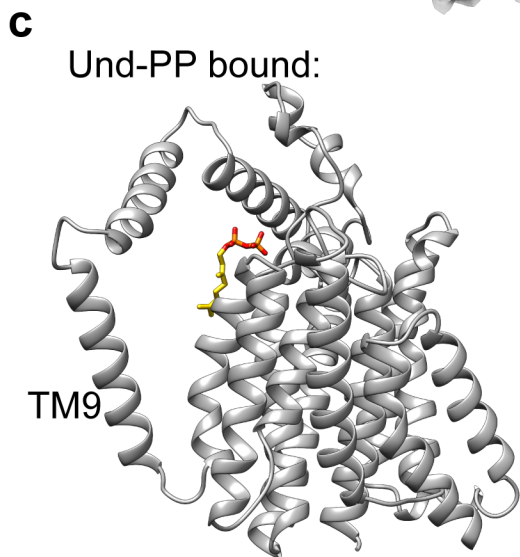
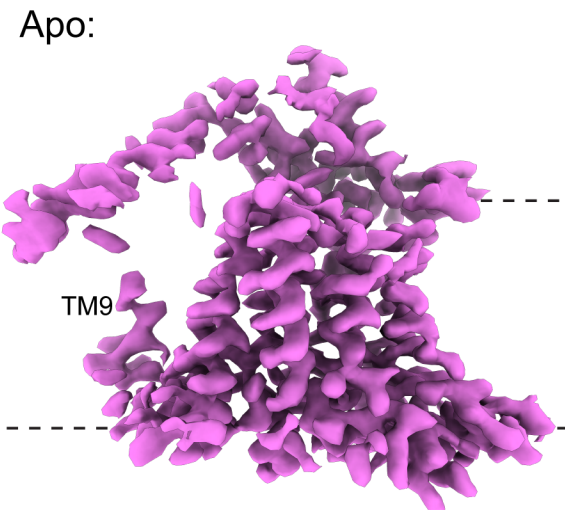
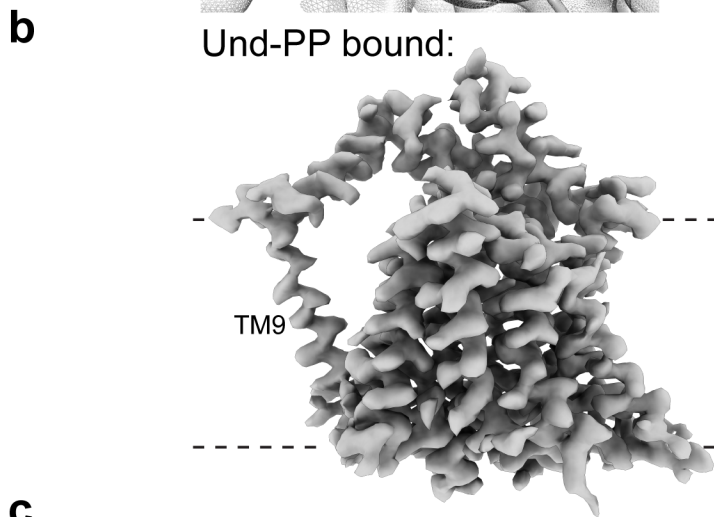
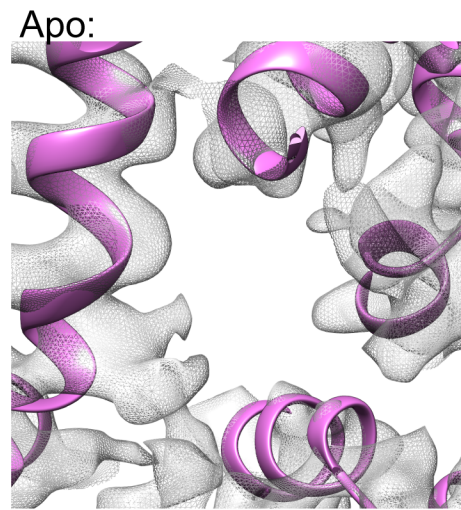
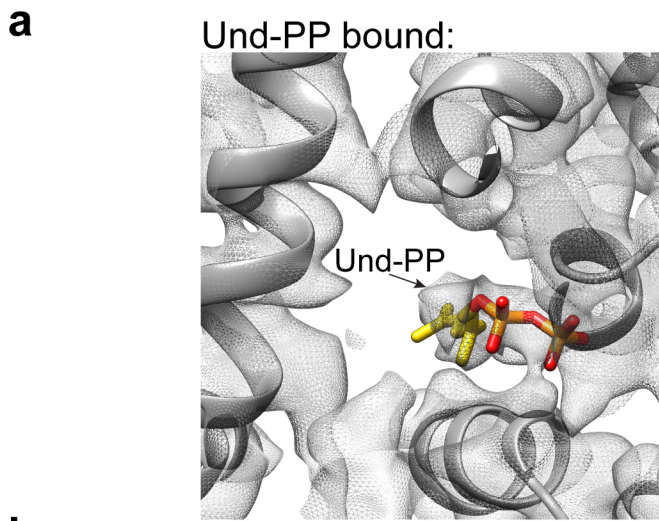




b

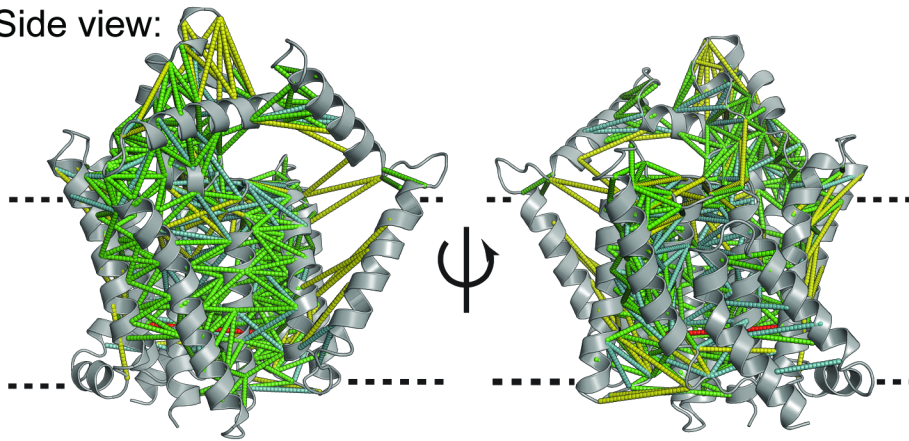
<i>CmWaaL</i>	<i>EcWaaL</i>
R28	K45
R92	K111
R139	R161
Q145	T168
I147	T170
R191	R215
R242	R265
R265	R288
H311	H336
H313	H338
E318	E343
Q378	D389
H383	A394



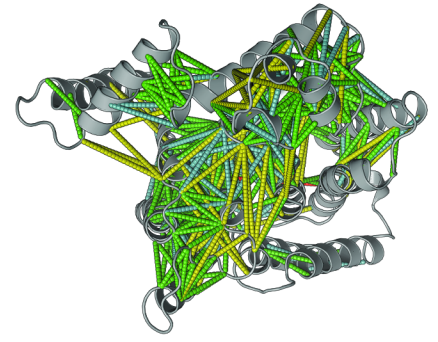
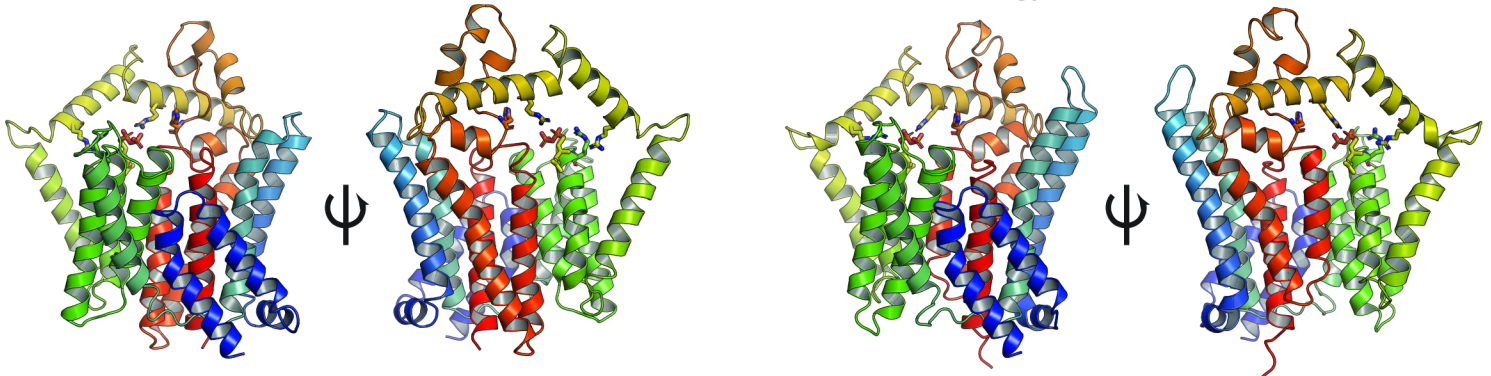


a

Side view:



Top view:

**b***CmWaaL* structure:*EcWaaL* homology model:**c***C. metallidurans*
E. coli

10 20 30 40 50 60
 NKL LSRMATV L V F A F P V L I L C V P R G A G V F L A G V G V L A L L G W R G M G R A W R E Y S K V M T P L A I
 S M I L E I I T Y I L C F F S M I I A F V D N T F S I K I Y N I T A I V C L L S . . . L I L R G R Q E N Y N I K N L I L

*C. metallidurans*
E. coli

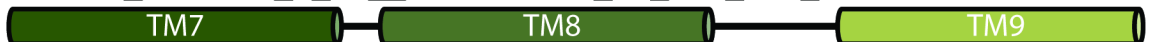
70 80 90 100 110
 A V L A F M L V Y V G S K L Y F H T P W N V I D N P S R T L L A I L T C W V I V R A A P N P A . . . W
 P L S I F L I G L L D L I W Y S A F K V D N S P F R A T Y H S Y L N T A K I F I F G S F I V F L T L T S Q L K S K K E S

*C. metallidurans*
E. coli

120 130 140 150 160 170
 L W R G I T V G L F L A L L I V G Y Q K F A L N I D R P S A W I Q A I A F A N M I A A L A L V G F A R P G D . . S R G T
 V L Y T L Y S L S F L I A G Y A M Y I N S I H E N D R I S F G V G T A T G A A Y S T M L I G I V S G V A I L Y T K K N H

*C. metallidurans*
E. coli

180 190 200 210 220 230
 H M E A W V N L L L G T M I L M L N G T R G A V V A M L V T S V P M L M I R Y R R F S V R M L I V A V C A V A T L A I G
 P F L F L L N S C A V L Y V L A L T Q T R A T L L L F P I C V A A L I A Y Y N K . S P K K F T S S I V L L I A I L A S

*C. metallidurans*
E. coli

240 250 260 270 280 290
 A Y M V P D S P V S K R V D D A V S E I Q M Y R Q G N I E T S V G V R L K I W H I G L Q Y F S E H P W T G V G V G Q F A
 I V I I F N K P I Q N R Y N E A L N D L N S Y T N A N S V T S L G A R L A M Y E I G L N I F I K S P F S F R S A E S R A

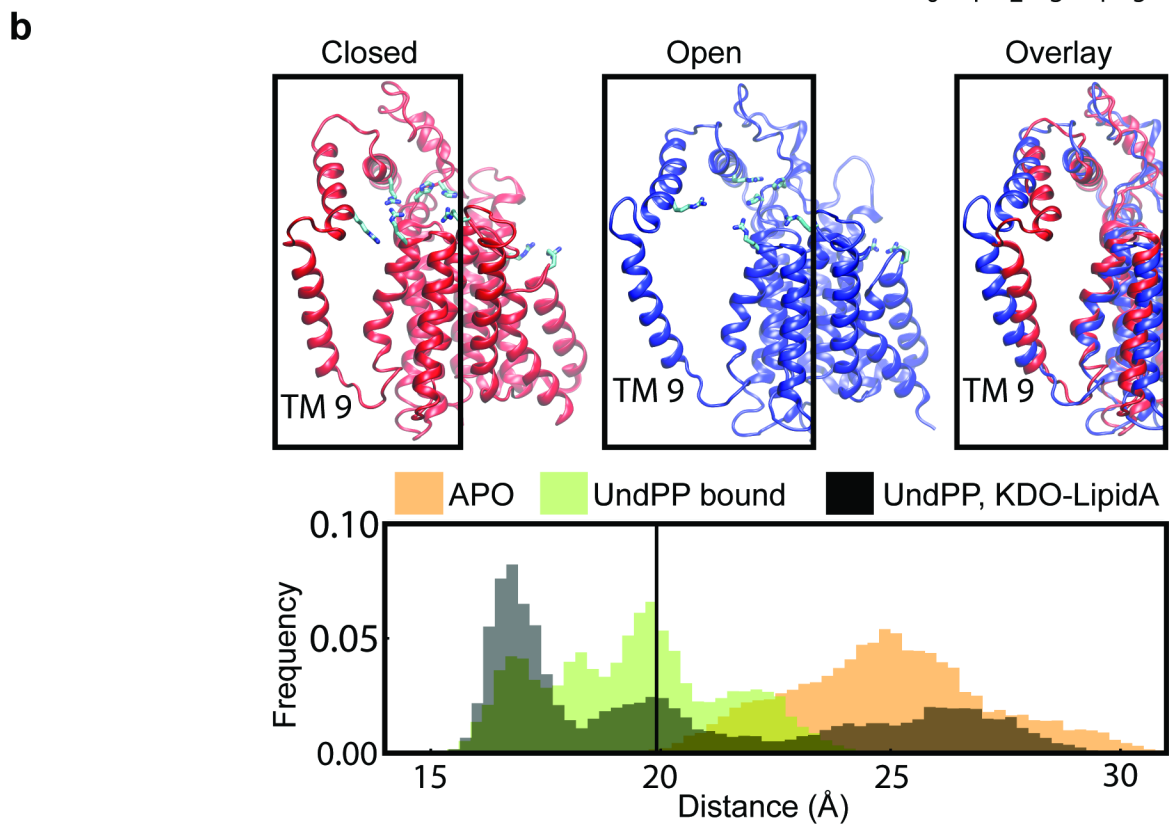
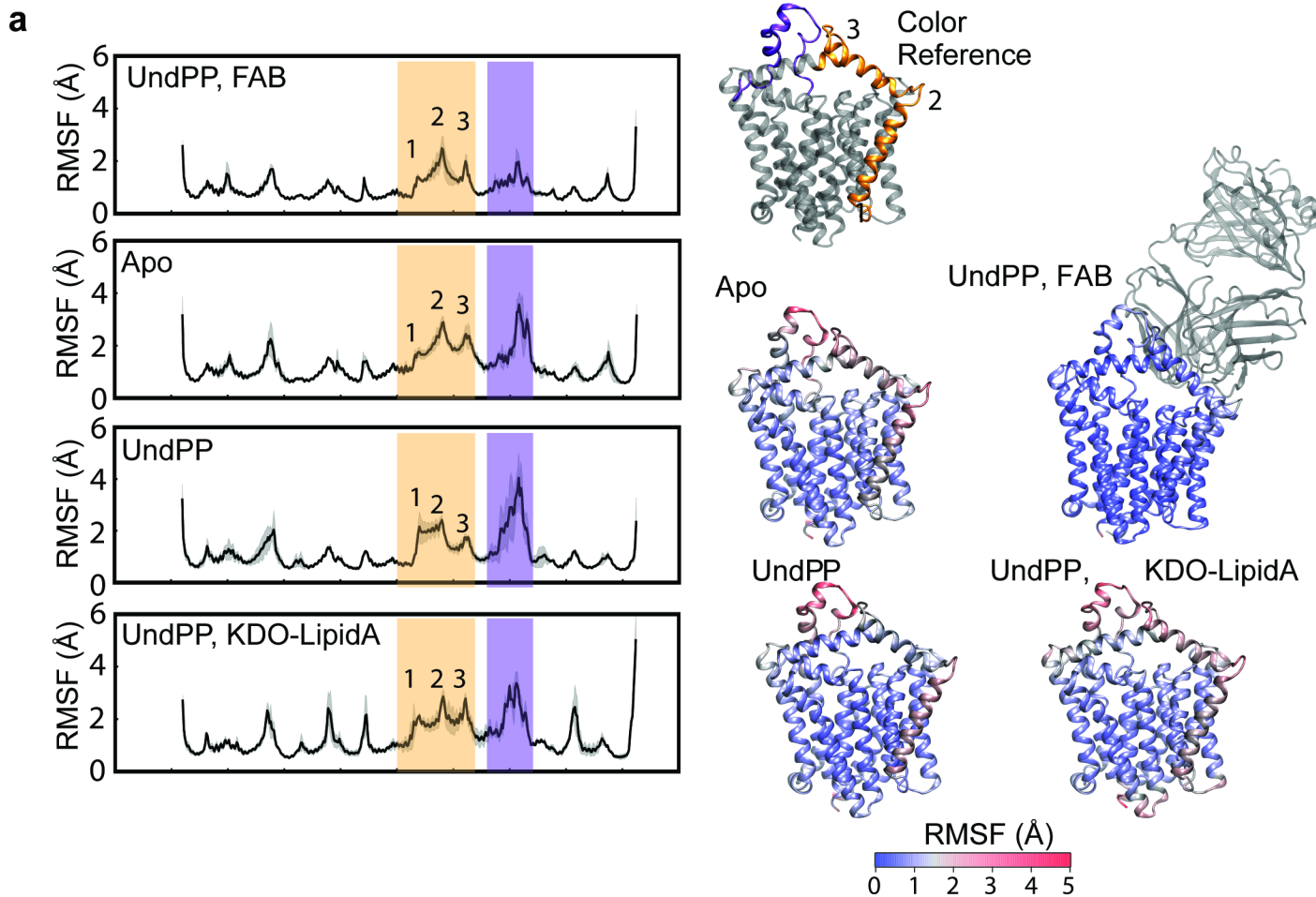
*C. metallidurans*
E. coli

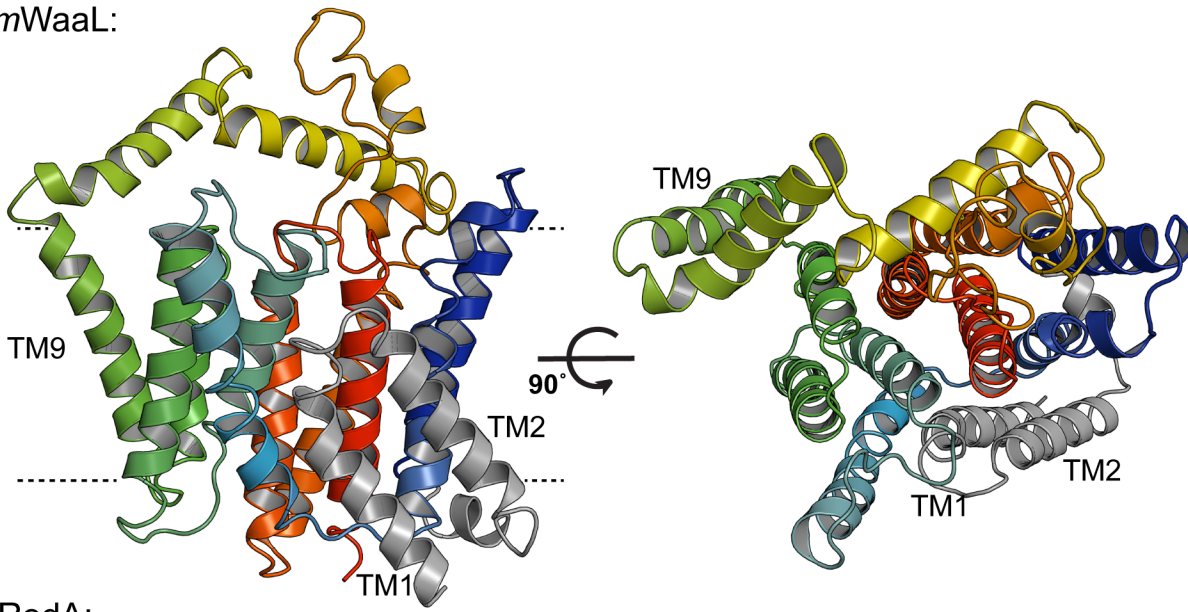
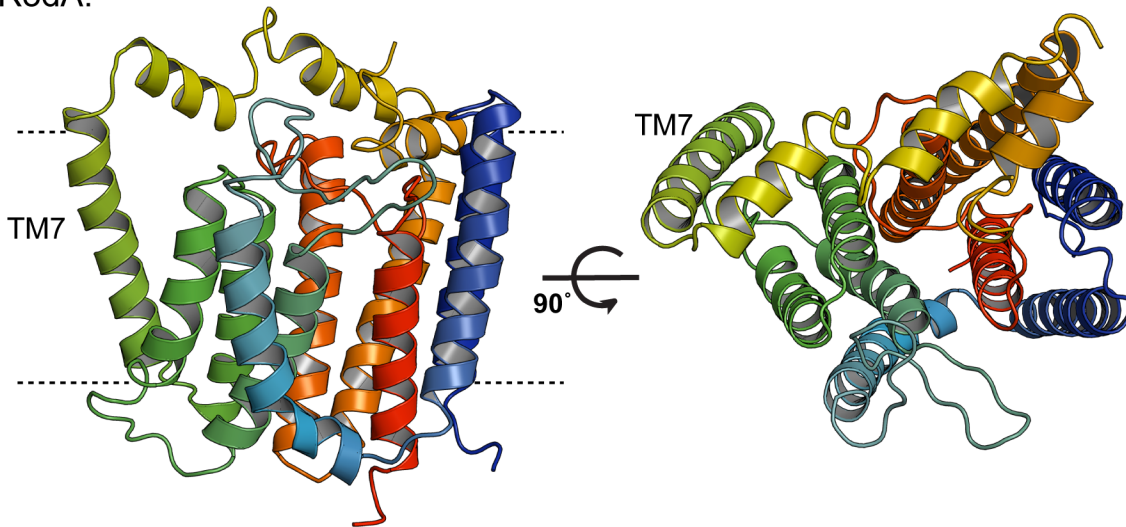
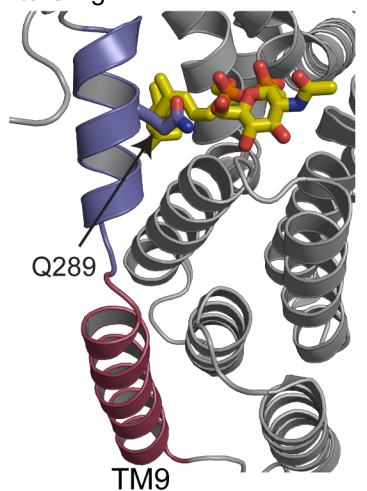
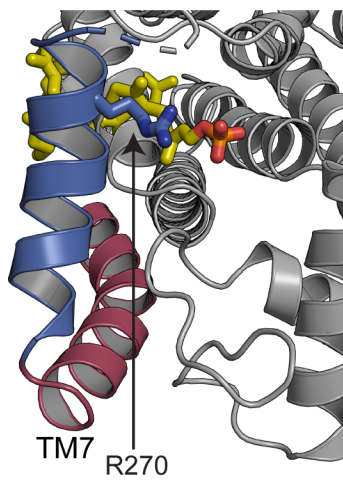
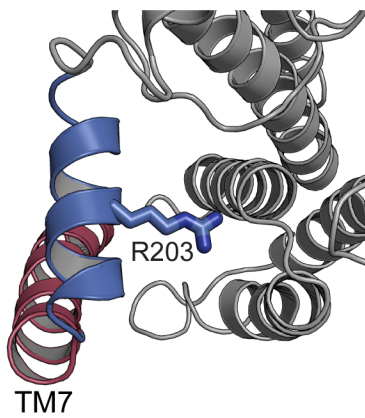
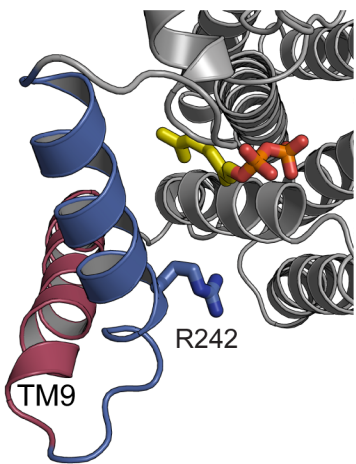
300 310 320 330 340
 R I L H A S . . E F C H E T K S L A C V L E H A H N D I V E A A S T T G I P G L M V M L G L F L V P A V L F A R A L R A
 E S M N L L V A E H N R L R G A L E F S N V H L H N E I E A G S L K G L M G I F S T L F L Y F S L F Y I A Y K K R . .

*C. metallidurans*
E. coli

350 360 370 380 390 400
 A R S L G N P Q G V S L G G A G L G V V M A S L I S G L T Q V T M A H Q A N V V F Y A G L I G L L L G M A G R E A H S
 A L G L L I L T L G I V G I G L S D V I I . W A R S I P I I I I S A I V L L L V I N N R N N T





a*CmWaaL*:*TtRodA*:**b**UndPP bound *CmWaaL*:Apo *TtRodA*:UndP bound *CmArnT*: $(\omega$ ZZZ)-PPC-GlcNAc bound to C/PglB:

1 **SI Guide**

2 Structural basis of Lipopolysaccharide Maturation by O-Antigen Ligase WaaL

3 Khuram U. Ashraf¹, Rie Nygaard¹, Owen N. Vickery^{2,3,#}, Satchal K. Erramilli^{4,#}, Carmen M.
4 Herrera^{5,#}, Thomas H. McConville^{6,#}, Vasileios I. Petrou^{7,8}, Sabrina I. Giacometti¹, Meagan
5 Belcher Dufresne¹, Kamil Nosol⁴, Allen P. Zinkle¹, Chris L.B. Graham², Michael Loukeris⁹,
6 Brian Kloss⁹, Karolina Skorupinska-Tudek¹⁰, Ewa Swiezewska¹⁰, David I. Roper^{2,1}, Oliver B.
7 Clarke^{1,11}, Anne-Catrin Uhlemann⁶, Anthony A. Kossiakoff⁴, M. Stephen Trent^{5*}, Phillip J.
8 Stansfeld^{2,3*} and Filippo Mancia^{1*}

9

10 ¹Department of Physiology and Cellular Biophysics, Columbia University Irving Medical
11 Center, New York, NY 10032, USA.

12 ²School of Life Sciences, University of Warwick, Coventry, CV4 7AL, UK.

13 ³Department of Chemistry, University of Warwick, Coventry, CV4 7AL, UK.

14 ⁴Department of Biochemistry and Molecular Biology, University of Chicago, Chicago, IL,
15 60637, USA.

16 ⁵Department of Infectious Diseases, College of Veterinary Medicine, University of Georgia,
17 Athens, GA, 30602, USA.

18 ⁶Department of Medicine, Division of Infectious Diseases, Columbia University Medical
19 Center, New York, New York, 10032, USA.

20 ⁷Department of Microbiology, Biochemistry, and Molecular Genetics, New Jersey Medical
21 School, Rutgers Biomedical Health Sciences, Newark, NJ, 07103, USA.

22 ⁸Center for Immunity and Inflammation, New Jersey Medical School, Rutgers Biomedical
23 Health Sciences, Newark, NJ, 07103, USA.

24 ⁹New York Consortium on Membrane Protein Structure, New York Structural Biology
25 Center, 89 Convent Avenue, New York, NY, 10027, USA.

26 ¹⁰Institute of Biochemistry and Biophysics, Polish Academy of Sciences, 02-106 Warsaw,
27 Poland.

28 ¹¹Department of Anesthesiology, Columbia University Irving Medical Center, New York,
29 NY, 10032, USA.

30

31 #These authors contributed equally.

32

33 *Correspondence to be addressed to: strent@uga.edu (M.S.T.),

34 Phillip.Stansfeld@warwick.ac.uk (P.J.S.), fm123@cumc.columbia.edu (F.M.)

35

36

37

38

39

40

41

42

43

44

45

46 **Table of Content:**

47 ***Red, dashed, boxes indicate how gels where cropped.**

48 **SI Figure 1 | Uncropped LPS assay gels from Main Figures. a,** LPS assay gel from [Fig. 2c](#)
49 showing analysis of *CmWaaL* ligase activity in whole cells. LPS gel showing O-antigen
50 extension in *C. metallidurans* expressing *CmWaaL* variants. With and empty plasmid as a
51 control. **b,** Functional analysis gel from [Fig. 4c](#) of *EcWaaL* ligase variants in whole cells by
52 LPS gel analysis. WaaL proteins were expressed from plasmid pWSK29 in the W3110
53 Δ waaL strain. With and empty plasmid as a control.

54 **SI Figure 2 | Uncropped LPS assay gels from Extended Data Figures. a,** LPS assay gel
55 from [Extended Data Fig. 1c](#) showing functional analysis of *CmWaaL* ligase activity in whole
56 cells, showing O-antigen ligase activity is abolished when the gene encoding WaaL is deleted
57 and activity is restored by plasmid complementation. **b,** Functional analysis of *EcWaaL*
58 ligase activity from [Extended Data Fig. 7a](#) carried out in whole cells by LPS gel analysis.
59 W3110 Δ waaL containing either empty vector pWSK29 (\emptyset), pWSK29::*EcWaaL* (WT) as
60 controls and pWSK19::*EcWaaL*- mutant variants to test for O-antigen ligase activity. **c,**
61 Functional analysis gel from [Extended Data Fig. 7e](#) showing *CmWaaL* ligase activity in
62 whole cells. *C. metallidurans* Δ waaL containing either empty vector pBBR1(\emptyset),
63 pBBR1::*CmWaaL* (WT) as controls for evaluating *CmWaaL*-variants for O-antigen extension.

64 **SI Figure 3 | Uncropped SDS-page gels from Extended Data Figures. a,** SDS-PAGE gel
65 from [Extended Data Fig. 1e](#) depicting *CmWaaL* purified in detergent, *CmWaaL* reconstituted
66 into nanodiscs (MSP1E3D1 and POPG), and *CmWaaL* reconstituted into nanodiscs
67 (MSP1E3D1 and POPG) with Fab (WaB10) bound. Molecular weight markers can also be
68 observed and are labelled. **b,** SDS-PAGE gels from [Extended Data Fig. 7c](#) of all *EcWaaL*
69 mutants used for LPS ligase analysis, that were purified to verify expression.

70 **SI Figure 4 | Uncropped TLC and Western Blot analysis from Extended Data Figures.**

71 **a**, TLC analysis from Extended Data Fig. 5d of detergent purified CmWaaL along with
72 suitable controls: POPG, Und-P, Und-PP and an unrelated control protein expressed in *E. coli*
73 were run in separate lanes. **b**, Western blot analysis, from Extended Data Fig. 7d, using a
74 mouse monoclonal anti-Flag antibody, of Flag purified WT *CmWaaL* and mutants, grown in
75 *C. metallidurans*, for testing in the O-antigen ligase assay. Red markers indicate molecular
76 weight markers.

77 **Supplementary Table 1 | Raw Single-point ELISA and Multi-point sAB ELISA data**

78

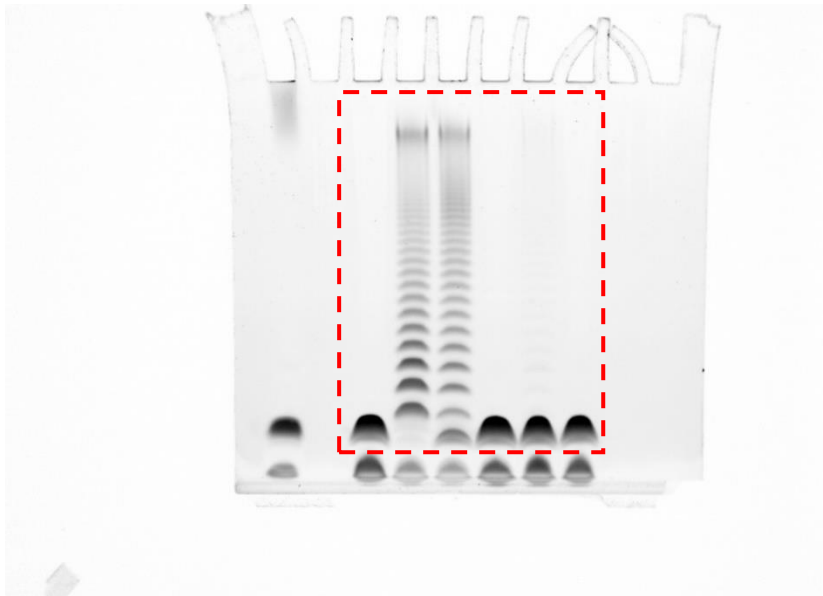
79

80

81

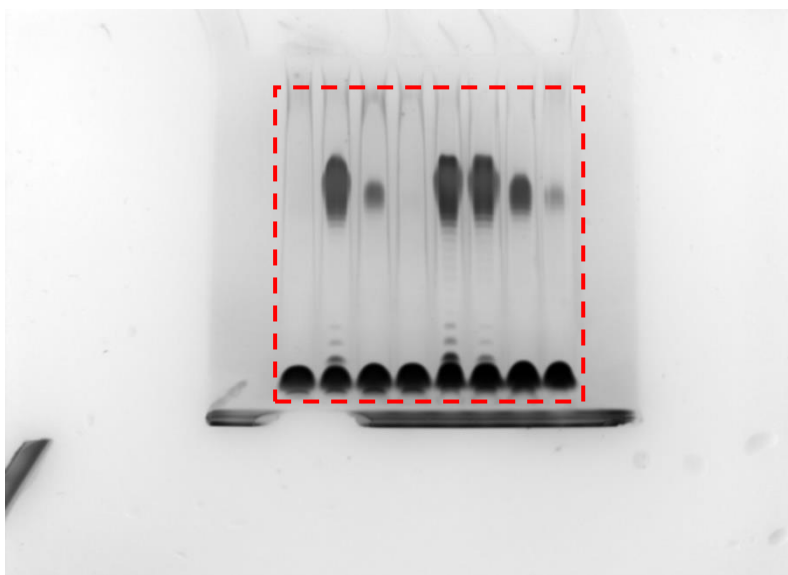
82

83



84

85 **Supplementary Figure 1a | Uncropped gel from Figure 2c.**

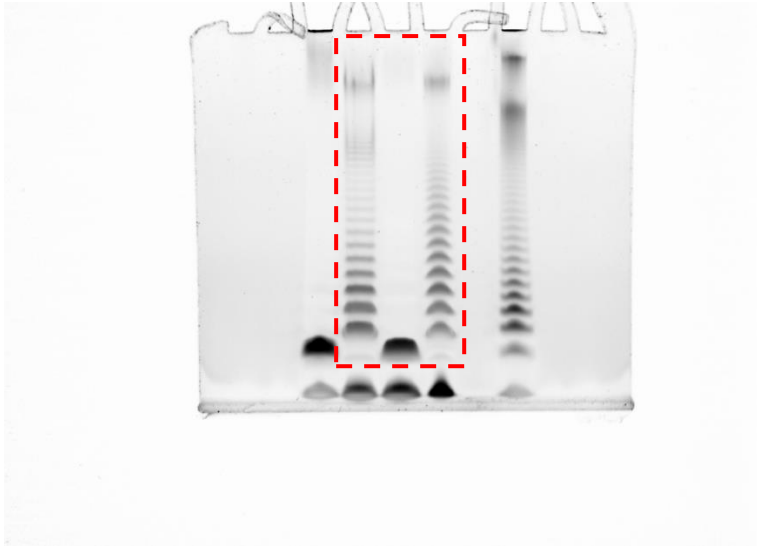


86

87 **Supplementary Figure 1b | Uncropped gel from Figure 4c.**

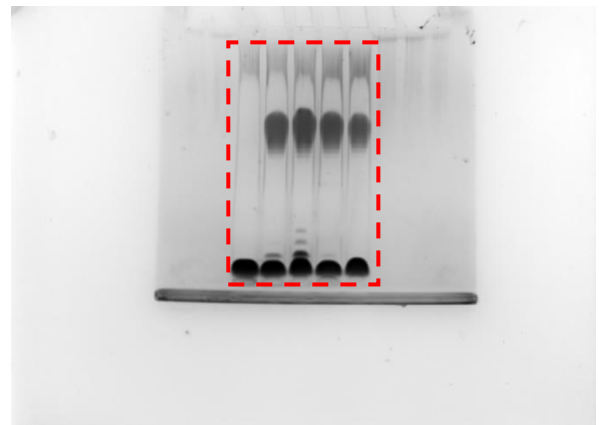
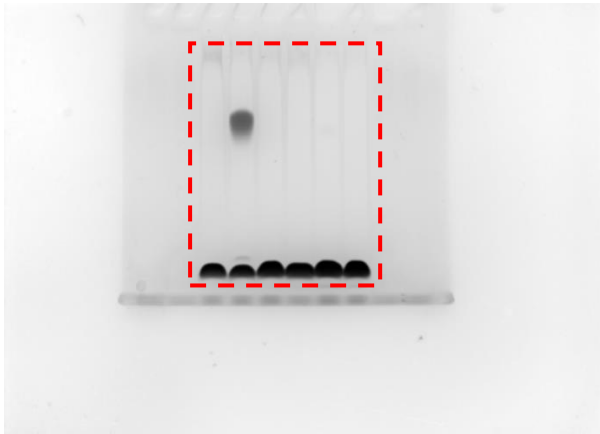
88

89

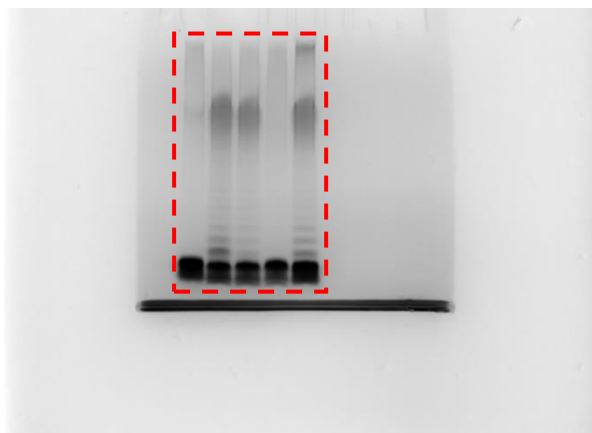


90

91 **Supplementary Figure 2a | Uncropped gel from Extended Data Fig. 1c**

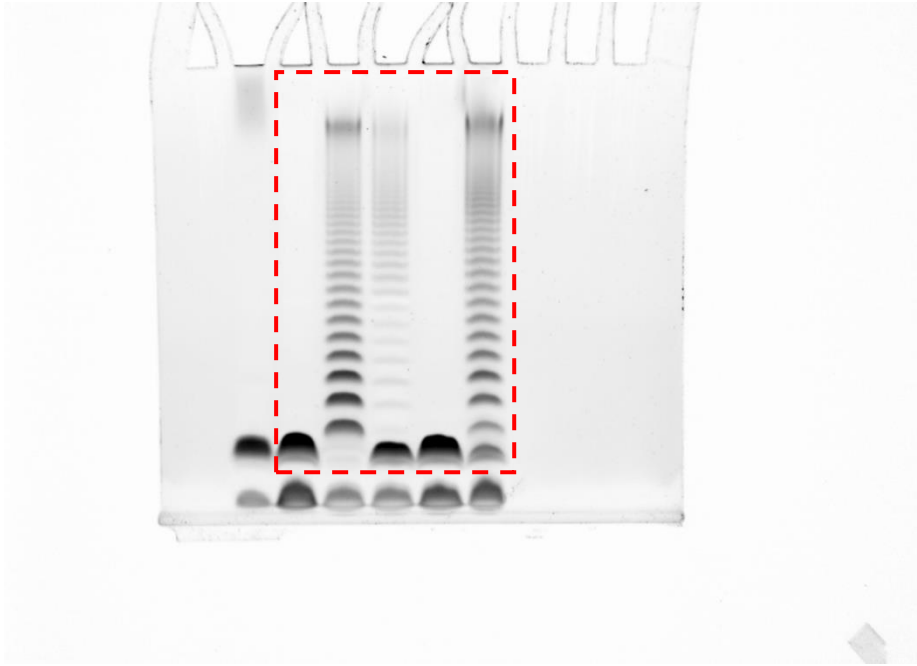


92



93

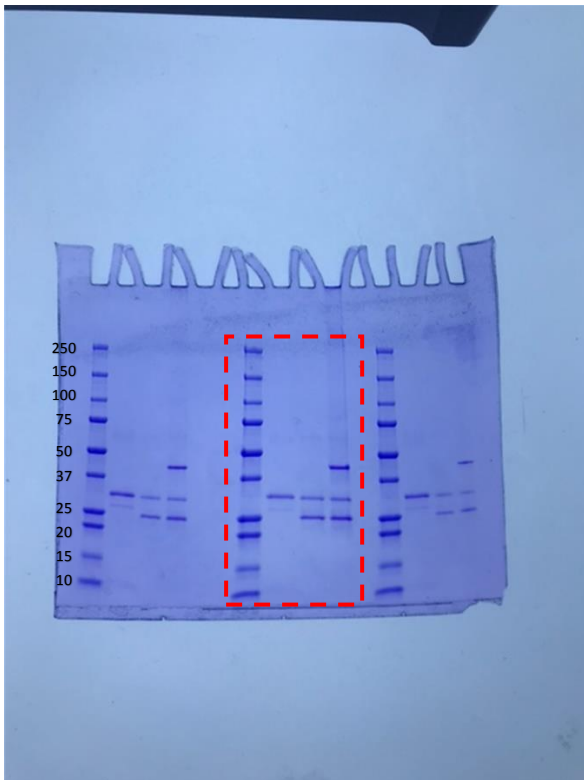
94 **Supplementary Figure 2b | Uncropped gels from Extended Data Fig. 7a**



95

96 **Supplementary Figure 2c | Uncropped gels from Extended Data Fig. 7e**

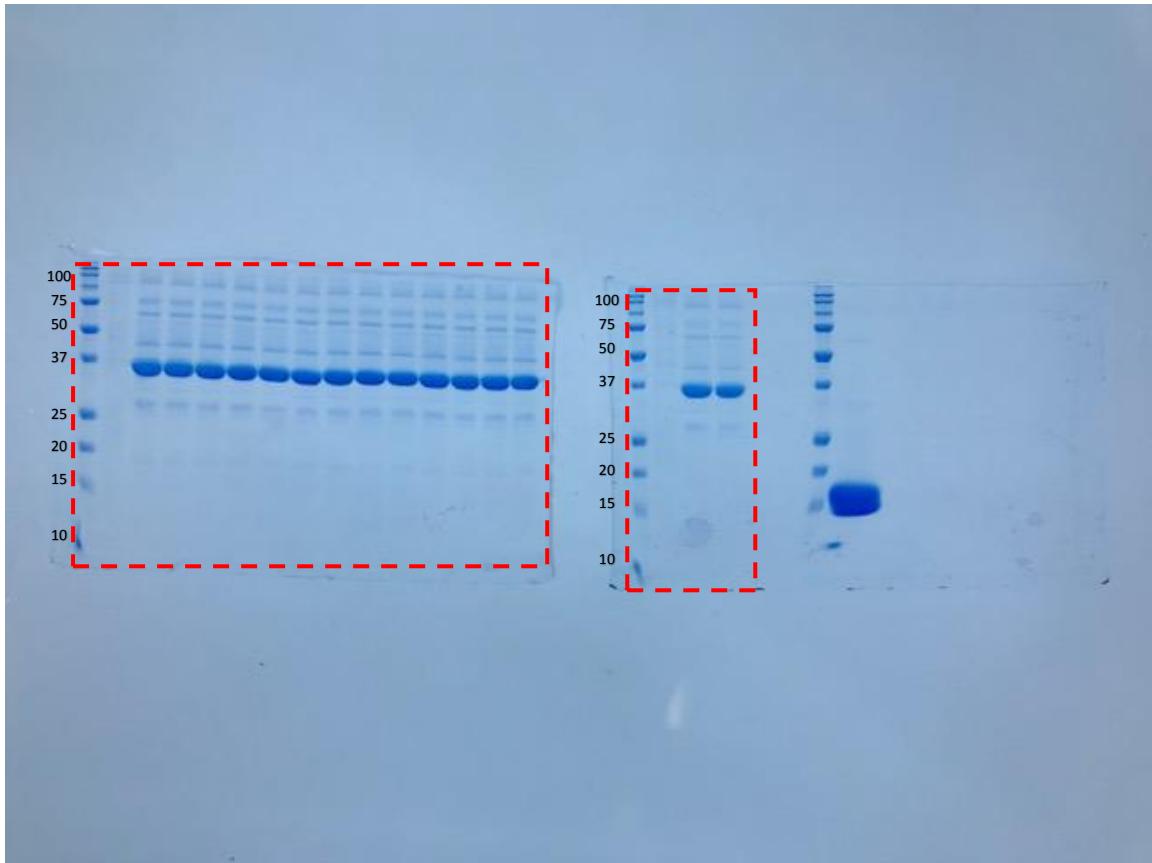
97



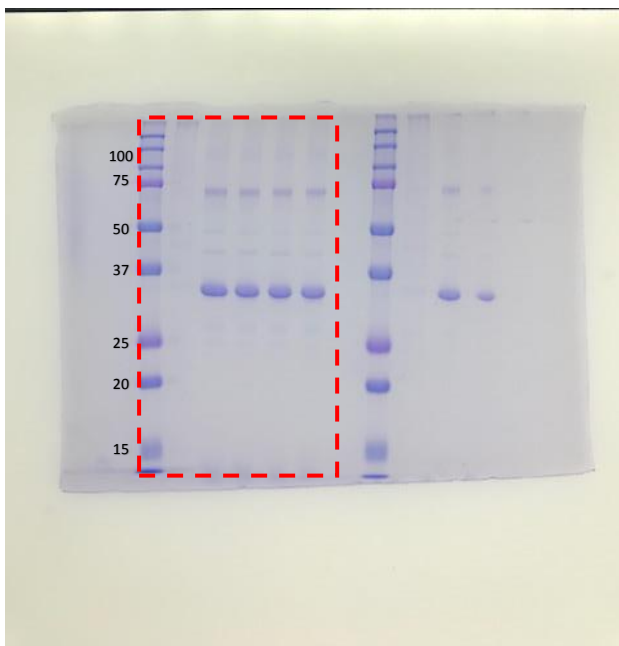
98

99 **Supplementary Figure 3a | Uncropped gel from Extended Data Fig. 1e**

100

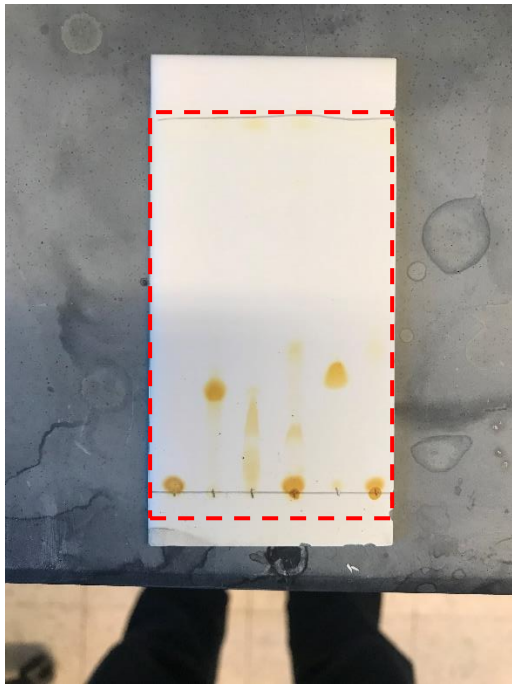


101



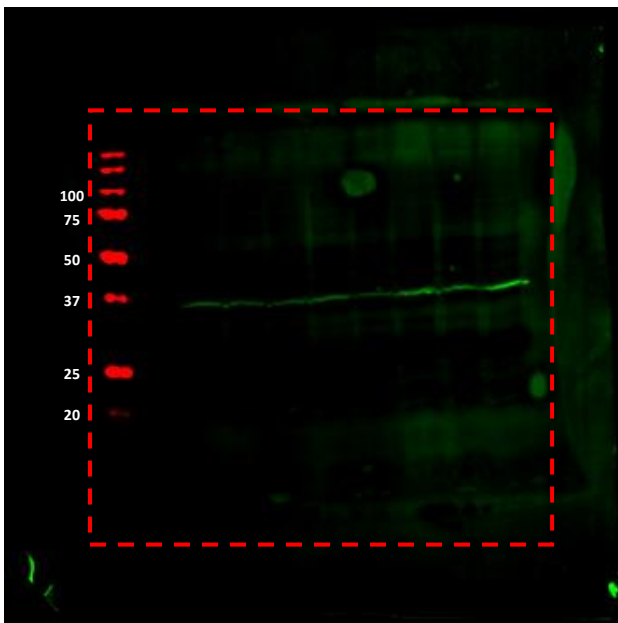
102

103 **Supplementary Figure 3b | Uncropped gel from Extended Data Fig. 7c**



104

105 **Supplementary Figure 4a | Uncropped gel from Extended Data Fig. 5d**



106

107 **Supplementary Figure 4b | Uncropped gel from Extended Data Fig. 7d**